Available online at www.sciencedirect.com
ScienceDirect
International Journal of Solids and Structures 43 (2006) 7424–7449
INTERNATIONAL JOURNAL OF SOLIDS and STRUCTURES
www.elsevier.com/locate/ijsolstr

Analytical elasto-creep model of interfacial thermal stresses and strains in trilayer assemblies

Hamid R. Ghorbani, Jan K. Spelt *

Department of Mechanical and Industrial Engineering, University of Toronto, 5 King's College Road, Toronto, Ont., Canada M5S 3G8

Received 23 June 2005; received in revised form 19 January 2006
Available online 14 February 2006

Communicated by David A. Hills

Abstract

A two-dimensional model has been developed for thermal stresses, elastic strains, creep strains, and creep energy density at the interfaces of short and long trilayer assemblies under both plane stress and plane strain conditions. Both linear (viscous) and non-linear creep constitutive behavior under static and cyclic thermal loading can be modeled for all layers. Interfacial stresses and strains are approximated using a combination of exact elasticity solutions and elementary strength of materials theories. Partial differential equations are linearized through a simple finite difference discretization procedure. The approach is mathematically straightforward and can be extended to include plastic behavior and problems involving external loads and a variety of geometries. The model can provide input data for thermal fatigue life prediction in solder or adhesive joints. For a typical solder joint, it is demonstrated that the predicted cyclic stress–strain hysteresis shows shakedown and a rapid stabilization of the creep energy dissipation per cycle in agreement with the predictions of finite element analysis.

Keywords: Trilayer; Layered beam; Laminated; Interfacial stress; Creep; Viscoelastic; Strain energy; Thermal cycling; Hysteresis; Ratcheting; Shakedown; Thermal stress; Thermal strain; Adhesive bond; Solder joint; Stress singularity

1. Introduction

Layered assemblies of dissimilar materials are a common feature of laminated structures, coatings and joints that are soldered, brazed or adhesively bonded. Under thermal loading such trilayer assemblies can suffer from unacceptable deformation (e.g. Madras et al., 1996), delamination and cracking because of expansivity and rigidity mismatch (e.g. Wang et al., 2000), residual stresses (e.g. Humfeld and Dillard, 1998), and creep-fatigue damage in structures with viscoelastic or viscoplastic materials (e.g. Qi et al., 2006).

* Corresponding author. Tel.: +1 416 978 5435.
E-mail address: spelt@mie.utoronto.ca (J.K. Spelt).

0020-7683/$ - see front matter
doi:10.1016/j.ijsolstr.2006.02.003

Interfacial thermal stress and strain distributions in layered structures have been analyzed using three main approaches: two-dimensional elasticity solutions, finite element (FE) analysis, and elementary beam theory. Many references can be found in the recent papers of Shen and Suresh (1996), Suhir (2001), Wen and Basaran (2004), and Ghorbani and Spelt (2005).

Two-dimensional elasticity solutions for interfacial thermal stresses were developed by Hayashi (1967), Bogy (1968), Zeyfang (1971), Chen et al. (1982), Yin (1991), Xie and Sitaraman (2000), Chen et al. (2003), Matsunaga (2004), and many others. This method usually leads to differential equations which must be solved numerically. It also results in an unrealistic singular stress field at the free edges of interfaces if an exact solution with strict adherence to the constitutive relations of linear elasticity is sought. In reality, the exact elasticity solution around free edges reflects the existence of a region with an intense stress or stress gradient (Yin, 1991).

Finite element analysis (FEA) has received wide attention in the analysis of layered assemblies. For instance, Mackerle (2002) gives a bibliography of 867 FEA papers in adhesive bonding, soldering, and brazing published in the period 1996–2002. Nevertheless, as shown by Glaser (1990), Basaran and Zhao (2001), Ghorbani and Spelt (2005), and many others, the predictions of elastic FEA are strongly mesh sensitive around the free corners of interlayers under thermal loading. This is a consequence of the underlying elasticity solutions which predict that peel stresses approach infinity at the free edges. Through the equilibrium equations this also affects the other stresses (Yin, 1991), causing elastic FE models to be accurate only away from the free edges.

The present elasto-creep analysis is based on the structural mechanics model of Ghorbani and Spelt (2005) for the thermal stresses in long and short trilayer assemblies. This model satisfies all equilibrium and compatibility requirements using compliances defined through elasticity solutions for both plane stress and plane strain conditions. The governing differential equations were solved using a straightforward finite difference procedure.

A few analytical models have been presented for the inelastic analysis of layered structures. Suhir (1986) proposed a closed-form structural mechanics solution for the elasto-plastic interfacial shear stress distribution in bilayer assemblies based on his structural mechanics approach and deformational plasticity. In this model, the plastic deformations due to other stress components (i.e. peel, axial, and out-of-plane) were neglected and equilibrium requirements for peel stresses were not met. For materials such as solder and polymeric adhesives, creep can be more detrimental than plastic deformation (Akay et al., 1997). Mirman and Knecht (1990) extended Suhir's model to account for creep strains due to only shear stresses in elongated bonded layers. However, the model neglected other stresses and creep deformations in trilayers.

Shen and Suresh (1995, 1996) developed analytical models for elasto-plastic and steady-state creep deformations in multi-layered materials during thermal cycling. The models were aimed at capturing residual stresses, stress relaxation and curvature reversal during monotonic temperature change. It was reported that the elasto-plastic model provided a better match with the experimental results during the heating phase, whereas the creep model was better during the cooling phase. It was assumed that stresses and strains varied only in the through-thickness direction (independent of longitudinal position), with the curvature being the same for all layers. This is an approximation since the radius of curvature is variable in both the longitudinal and transverse directions from one layer to another (Ghorbani and Spelt, 2005).

Madras et al. (1996), in an attempt to explain the permanent deformations observed experimentally in adhesively bonded optical coatings during thermal cycling, modeled the adhesive using a simple Maxwell (spring-dashpot) element with a temperature-dependent viscosity. Humfeld and Dillard (1998) developed an analytical Maxwell-type model to calculate the residual stresses and stress relaxation in polymeric materials bonding to stiff elastic substrates subject to thermal cycling. The model treats the interlayer as a bulk Maxwell element (i.e. a spring and a dashpot in series), assuming that the axial stress is the only component of stress in the interlayer and that it is constant. The model is therefore applicable to the midpoint of the adhesive layer, where the interfacial stresses vanish. Using FEA, Dillard et al. (2003) provided further insights into shrinkage and hysteresis in viscoelastic adhesive joints under cyclic thermal loads.

As mentioned above, the present 2D elasto-creep analytical model for trilayer assemblies extends an earlier elastic model for interfacial thermal stresses (Ghorbani and Spelt, 2005). The model is applicable to trilayers with any aspect ratio (i.e. both long and short) under either plane stress or plane strain conditions, and can be used with either a linear (viscous) or non-linear creep model for any of the three layers. Sample calculations

illustrate comparisons with FE models for the time-dependent distribution of elastic and creep interfacial stresses and strains during thermal cycling.

2. Creep rate under plane stress and plane strain conditions

Assuming a linear relationship between the creep strain rate and stress (i.e. viscous or linear creep) the normal and shear creep strain rates under plane stress and plane strain conditions can be defined as (Dowling, 1999)

$$\dot{\varepsilon}_{x\mathrm{C}}(t) = \frac{1}{\beta(t)}[\sigma_x(t) - 0.5(\sigma_y(t) + \sigma_z(t))] \tag{1}$$

$$\dot{\varepsilon}_{y\mathrm{C}}(t) = \frac{1}{\beta(t)}[\sigma_y(t) - 0.5(\sigma_x(t) + \sigma_z(t))] \tag{2}$$

$$\dot{\varepsilon}_{z\mathrm{C}}(t) = \frac{1}{\beta(t)}[\sigma_z(t) - 0.5(\sigma_x(t) + \sigma_y(t))] \tag{3}$$

$$\dot{\varepsilon}_{xy\mathrm{C}}(t) = \frac{3}{\beta(t)}\tau_{xy}(t) \tag{4}$$

where t denotes time, and β is the tensile viscosity of the material. These relations are analogous to Hooke's law except that they involve strain rates and Poisson's ratio, ν, is replaced by 0.5, E by β, and G by $\beta/3$. In other words, it is assumed that creep deformation occurs at constant volume and is uninfluenced by hydrostatic stress, that the principal axes of stress and creep strain are coincident, and that the material is isotropic (Findley et al., 1979). Note in Eqs. (1)–(3) that $\sigma_z(t)$ is zero under plane stress condition, but $\dot{\varepsilon}_z(t)$ is not zero under plane strain condition if elastic and thermal strains are present (see Eq. (51)).

The viscous (linear) creep concept has been used in many analytical models; e.g. Hibbeler and Mura (1969), Mirman and Knecht (1990), Madras et al. (1996), Humfeld and Dillard (1998), and Dillard et al. (2003). It was shown by Yang (1997) that the creep controlled by grain boundary viscous flow may have the same mechanism and order as does that controlled by grain boundary diffusion. Dutta et al. (2003) also presented an

Table 1
Material properties (Qi et al., 2004) and dimensions of example trilayers (symbols and layers defined in Fig. 1 and Section 3.1)

Example trilayer	L (mm)	Layers (3/2/1)	h (mm)	E (GPa)	ν	CTE (ppm/°C)	Creep constitutive law[a] ($\dot{\varepsilon}_{\mathrm{cr}}$) with θ (K) and σ[b] (Pa)
1	0.76 (Short)	Resistor	0.65	131	0.30	2.8	$4.68\times10^{-11}\times441{,}000\sigma\exp[-5412/\theta]$
		SAC	0.12	25 °C: 46 50 °C: 44 100 °C: 41	0.30	17	
		FR-4	1.23	22	0.28	19	
2	0.76 (Short)	Resistor	0.65	131	0.30	2.8	$441{,}000[\sinh(5\times10^{-9}\sigma)]^{4.2}\exp[-5412/\theta]$
		SAC	0.12	25 °C: 46 50 °C: 44 100 °C: 41	0.30	17	
		FR-4	1.23	22	0.28	19	
3	0.76 (Short)	Resistor	0.65	131	0.30	2.8	$[926(508-\theta)/\theta]\exp[-6360/\theta]$
		SnPb	0.12	$75.940–0.152\times\theta$ (K)	0.40	22	$\times\{\sinh[\sigma/(37.78\times10^{6}-74{,}414\theta)]\}^{3.3}$
		FR-4	1.23	22	0.28	19	
4	3.8 (Long)	Resistor	0.65	131	0.30	2.8	$441{,}000[\sinh(5\times10^{-9}\sigma)]^{4.2}\exp[-5412/\theta]$
		SAC	0.12	25°C: 46 50 °C: 44 100 °C: 41	0.30	17	
		FR-4	1.23	22	0.28	19	

[a] $\beta(\theta) = \sigma/\dot{\varepsilon}_{\mathrm{cr}} = 1/\{4.68\times10^{-11}\times441{,}000\exp[-5412/\theta]\}$ in the linear creep model of Example 1.
[b] σ is to be replaced with the von Mises stress.

interesting discussion on how the interfacial thermal creep in multi-component material systems, such as in metal–matrix composites and microelectronic interconnects, can be described using linear creep based on both interfacial shear and peeling stresses. In general, however, it is more accurate to use a non-linear creep constitutive relation in multi-layered structures (Lewis et al., 2003), particularly if stresses are relatively large (Shen and Suresh, 1996).

In order to extend the above equations to cases where the creep constitutive law is non-linear (e.g. dislocation glide creep, power-law creep, power-law breakdown creep, diffusional flow creep), β may be interpreted as a secant modulus on a stress versus strain rate plot (Dowling, 1999):

$$\beta(t) = \frac{S(t)}{\dot{\varepsilon}_{\mathrm{cr}}(t)} \tag{5}$$

where S is the von Mises stress as defined by Eq. (54) below, and $\dot{\varepsilon}_{\mathrm{cr}}$ is the corresponding creep strain rate of the material (Table 1).

3. Problem formulation

3.1. Free-body diagram

Fig. 1 shows a plane view of a trilayer assembly of length $L = 2l$. The Poisson ratio, elastic modulus, coefficient of thermal expansion, thickness, and extensional viscosity of each layer respectively, are ν_j, $E_j(t)$, $\alpha_j(t)$, h_j, and $\beta_j(t)$ where the index $j = 1,2,3$ denotes the layers. The elastic and creep rigidities of each layer are assumed to be temperature-dependent. Under a uniform temperature change, $\Delta\theta(t)$, the layers may undergo elastic and inelastic creep deformations. The interfacial shear stress, $\tau_{xym}(x,t)$, and peel stresses, $\sigma_{ym}(x,t)$, vary with the interface number, $m = 1,2$. The axial, transverse shear and bending loads acting at the midplane of each layer cross-section are, respectively, $T_j(x,t)$, $V_j(x,t)$, and $M_j(x,t)$. The axial and transverse shear forces are due to the interlaminar shear and peel stresses, respectively. Together with the bending moments, they vanish at the free ends of the assembly.

The interlaminar shear stresses, created by the mismatch of the coefficient of thermal expansion (CTE) of the layers, will vanish at the ends of the assembly. The peel stresses are due to differences in the elastic and creep rigidities of the adjacent layers and must be self-equilibrating.

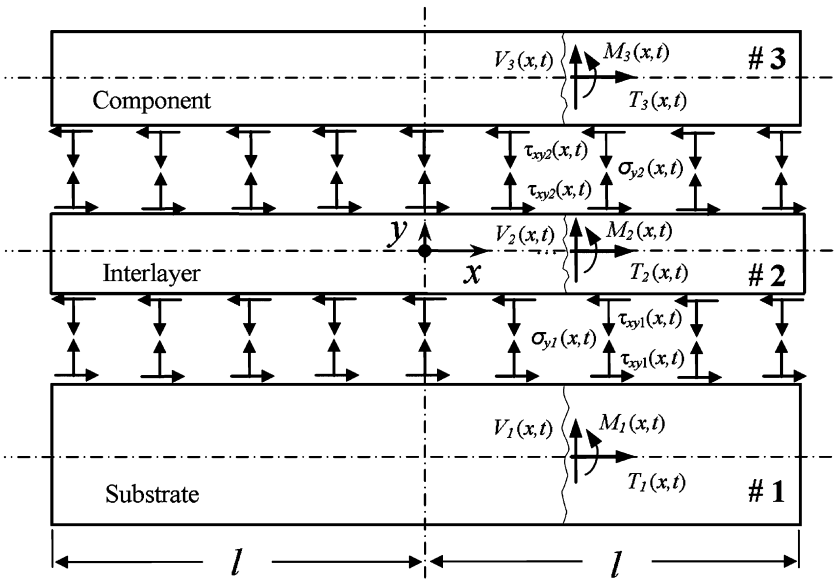

Fig. 1. Free-body diagram of a trilayer subject to a uniform time-dependent temperature change. $z = 0$ corresponds to the x–y plane of symmetry along the centreline of the trilayer assembly.

3.2. Equilibrium equations

The equilibrium of horizontal forces at each cross-section implies that (Fig. 1):

$$T_1(x,t) = -\int_{-l}^{x} \tau_{xy1}(\xi,t)\,\mathrm{d}\xi \tag{6}$$

$$T_2(x,t) = \int_{-l}^{x} [\tau_{xy1}(\xi,t) - \tau_{xy2}(\xi,t)]\,\mathrm{d}\xi = -[T_1(x,t) + T_3(x,t)] \tag{7}$$

$$T_3(x,t) = \int_{-l}^{x} \tau_{xy2}(\xi,t)\,\mathrm{d}\xi \tag{8}$$

Similarly, equilibrium of the transverse forces at each cross-section gives (Fig. 1):

$$V_1(x,t) = -\int_{-l}^{x} \sigma_{y1}(\xi,t)\,\mathrm{d}\xi \tag{9}$$

$$V_2(x) = \int_{-l}^{x} [\sigma_{y1}(\xi,t) - \sigma_{y2}(\xi,t)]\,\mathrm{d}\xi = -[V_1(x,t) + V_3(x,t)] \tag{10}$$

$$V_3(x,t) = \int_{-l}^{x} \sigma_{y2}(\xi,t)\,\mathrm{d}\xi \tag{11}$$

Lastly, equilibrium of the bending moments at each cross-section yields (Fig. 1):

$$M_1(x,t) = -\frac{h_1}{2} T_1(x,t) - \int_{-l}^{x} V_1(\xi,t)\,\mathrm{d}\xi \tag{12}$$

$$M_2(x,t) = \frac{h_2}{2}[T_3(x,t) - T_1(x,t)] + \int_{-l}^{x} [V_1(\xi,t) + V_3(\xi,t)]\,\mathrm{d}\xi \tag{13}$$

$$M_3(x,t) = \frac{h_3}{2} T_3(x,t) - \int_{-l}^{x} V_3(\xi,t)\,\mathrm{d}\xi \tag{14}$$

Finally, from Eqs. (6)–(14), the condition that these forces and moments must be zero at $x = \pm l$ yields:

$$\int_{-l}^{l} \tau_{xym}(\xi,t)\,\mathrm{d}\xi = \int_{-l}^{l} \sigma_{ym}(\xi,t)\,\mathrm{d}\xi = \int_{-l}^{l} V_j(\xi,t)\,\mathrm{d}\xi = 0 \tag{15}$$

implying that the interfacial shear and peel stresses, and transverse shear forces remain self-equilibrating.

3.3. Compatibility of horizontal deformations

The time-dependent longitudinal displacements of the component, interlayer and substrate in the neighborhood of each interface, $u_j^m(x,t)$, are comprised of three terms; free thermal expansion with respect to the assembly vertical centerline, elastic deformations, $u_{j\mathrm{E}}^m(x,t)$, and creep deformations, $u_{j\mathrm{C}}^m(x,t)$:

$$u_j^m(x,t) = \alpha_j^*(t)\Delta\theta(t)x + u_{j\mathrm{E}}^m(x,t) + \int_0^t \dot{u}_{j\mathrm{C}}^m(x,s)\,\mathrm{d}s \tag{16}$$

where $\alpha_j^*(t)$ is the effective coefficient of thermal expansion equal to $\alpha_j(t)$ if the layer is subject to creep deformation in both plane stress and plane strain. If the layer is subject to elastic deformation only, $\alpha_j^*(t)$ equals $\alpha_j(t)$ in plane stress and $(1+\nu_j)\alpha_j(t)$ under plane strain. The elastic interfacial deformations of Eq. (16) may be expressed as (Ghorbani and Spelt, 2005):

$$u_{1\mathrm{E}}^1(x,t) = \lambda_{1\mathrm{E}}(t)\int_0^x T_1(\xi,t)\,\mathrm{d}\xi + \eta_{1\mathrm{E}}(t)[\tau_{xy1}(x,t) - d_1\tau_{xy1}''(x,t)] - \frac{1}{2}\frac{h_1}{D_{1\mathrm{E}}(t)}\int_0^x M_1(\xi,t)\,\mathrm{d}\xi \tag{17}$$

$$u_{2\mathrm{E}}^1(x,t) = \lambda_{2\mathrm{E}}(t)\int_0^x T_2(\xi,t)\,\mathrm{d}\xi - \eta_{2\mathrm{E}}(t)[\tau_{xy1}(x,t) - d_2\tau_{xy1}''(x,t)] + \frac{1}{2}\frac{h_2}{D_{2\mathrm{E}}(t)}\int_0^x M_2(\xi,t)\,\mathrm{d}\xi \tag{18}$$

$$u^2_{2E}(x,t) = \lambda_{2E}(t)\int_0^x T_2(\xi,t)\,d\xi + \eta_{2E}(t)[\tau_{xy2}(x,t) - d_2\tau''_{xy2}(x,t)] - \frac{1}{2}\frac{h_2}{D_{2E}(t)}\int_0^x M_2(\xi,t)\,d\xi \tag{19}$$

$$u^2_{3E}(x,t) = \lambda_{3E}(t)\int_0^x T_3(\xi,t)\,d\xi - \eta_{3E}(t)[\tau_{xy2}(x,t) - d_3\tau''_{xy2}(x,t)] + \frac{1}{2}\frac{h_3}{D_{3E}(t)}\int_0^x M_3(\xi,t)\,d\xi \tag{20}$$

where $\lambda_{jE}(t)$ is the axial compliance, $\eta_{jE}(t)$ is the shear compliance, and $D_{jE}(t)$ is the flexural rigidity of the jth layer subject to elastic deformation as defined in Ghorbani and Spelt (2005) for both plane stress and plane strain conditions. In Eqs. (17)–(20), the first terms are longitudinal displacements due to the axial loads, while the second and third terms capture the deformations due to interfacial shear and bending, respectively.

The present model can be regarded as "non-local" as defined by Ru (2002) since it includes the effect of $\tau''_{xym}(x)$ in the interfacial shear displacements. It was seen in Ghorbani and Spelt (2005) that this is essential if the elastic model is to predict the large shear stress gradient near the free ends, enabling the interfacial shear stresses to vanish at the free surfaces. It was also seen that the shear parameters d_j control the shape of the shear stress gradient close to the free ends of the interfaces, and that $h_j^2/1000\pi^2$ was a phenomenologically acceptable value for d_j under elastic deformations. As discussed in Section 5.2 below, d_j approaches zero under elasto-creep conditions as the creep deformations are accumulated in the interfacial region.

Similarly, the rate of interfacial creep deformation in Eq. (16) can be defined as

$$\dot{u}^1_{1C}(x,t) = \lambda_{1C}(t)\int_0^x T_1(\xi,t)\,d\xi + \eta_{1C}(t)\tau_{xy1}(x,t) - \frac{1}{2}\frac{h_1}{D_{1C}(t)}\int_0^x M_1(\xi,t)\,d\xi \tag{21}$$

$$\dot{u}^1_{2C}(x,t) = \lambda_{2C}(t)\int_0^x T_2(\xi,t)\,d\xi - \eta_{2C}(t)\tau_{xy1}(x,t) + \frac{1}{2}\frac{h_2}{D_{2C}(t)}\int_0^x M_2(\xi,t)\,d\xi \tag{22}$$

$$\dot{u}^2_{2C}(x,t) = \lambda_{2C}(t)\int_0^x T_2(\xi,t)\,d\xi + \eta_{2C}(t)\tau_{xy2}(x,t) - \frac{1}{2}\frac{h_2}{D_{2C}(t)}\int_0^x M_2(\xi,t)\,d\xi \tag{23}$$

$$\dot{u}^2_{3C}(x,t) = \lambda_{3C}(t)\int_0^x T_3(\xi,t)\,d\xi - \eta_{3C}(t)\tau_{xy2}(x,t) + \frac{1}{2}\frac{h_3}{D_{3C}(t)}\int_0^x M_3(\xi,t)\,d\xi \tag{24}$$

where $\lambda_{jC}(t)$, $\eta_{jC}(t)$, and $D_{jC}(t)$ are, respectively, the axial and shear creep compliances and the creep flexural rigidity of the jth layer. These terms are derived in Appendix A for both plane stress and plane strain conditions. In Eqs. (21)–(24), the first terms are longitudinal creep displacements due to the axial loads and the second and third terms are interfacial shear and flexural creep deformations, respectively. Note that the non-local term $\tau''_{xym}(x)$ is no longer used since the creep displacements can be described accurately without it (Appendix A).

Substituting for the bending moments from Eqs. (12)–(14), using compatibility of the horizontal displacements at each interface (i.e. $u^1_1(x,t) = u^1_2(x,t)$ and $u^2_2(x,t) = u^2_3(x,t)$) and differentiating with respect to x leads to the following system of coupled time-dependent integro-differential equations:

$$\begin{aligned}
&-k_{1E}(t)T_1(x,t) + k_{2E}(t)T_3(x,t) - k_{3E}(t)\tau'_{xy1}(x,t) + k_{6E}(t)\tau'''_{xy1}(x,t) + k_{8E}(t)\int_{-l}^x V_1(\xi,t)\,d\xi \\
&\quad + k_{9E}\int_{-l}^x V_3(\xi,t)\,d\xi + \int_0^t\Big[-k_{1C}(s)T_1(x,s) + k_{2C}(s)T_3(x,s) - k_{3C}(s)\tau'_{xy1}(x,s) \\
&\quad + k_{8C}(s)\int_{-l}^x V_1(\xi,s)\,d\xi + k_{9C}(s)\int_{-l}^x V_3(\xi,s)\,d\xi\Big]\,ds = [\alpha^*_1(t) - \alpha^*_2(t)]\Delta\theta(t)
\end{aligned} \tag{25}$$

$$\begin{aligned}
&-k_{2E}(t)T_1(x,t) + k_{4E}(t)T_3(x,t) - k_{5E}(t)\tau'_{xy2}(x,t) + k_{7E}(t)\tau'''_{xy2}(x,t) + k_{9E}(t)\int_{-l}^x V_1(\xi,t)\,d\xi \\
&\quad + k_{10E}(t)\int_{-l}^x V_3(\xi,t)\,d\xi + + \int_0^t\Big[-k_{2C}(s)T_1(x,s) + k_{4C}(s)T_3(x,s) - k_{5C}(s)\tau'_{xy2}(x,s) \\
&\quad + k_{9C}(s)\int_{-l}^x V_1(\xi,s)\,d\xi + k_{10C}(s)\int_{-l}^x V_3(\xi,s)\,d\xi\Big]\,ds = [\alpha^*_2(t) - \alpha^*_3(t)]\Delta\theta(t)
\end{aligned} \tag{26}$$

where the elastic stiffnesses $k_{1E}(t)$–$k_{10E}(t)$ are given in Ghorbani and Spelt (2005). The creep compliances $k_{1C}(t)$–$k_{10C}(t)$ are exactly the same as the corresponding elastic compliances except that $E_j(t)$ is replaced by $\beta_j(t)$ and v_j by 0.5. Substituting for the axial forces from Eqs. (6) and (8) and differentiating yields:

$$\left[k_{6E}(t)\frac{d^4}{dx^4}-k_{3E}(t)\frac{d^2}{dx^2}+k_{1E}(t)\right]\tau_{xy1}(x,t)+k_{2E}(t)\tau_{xy2}(x,t)+k_{8E}(t)V_1(x,t)+k_{9E}(t)V_3(x,t)+\int_0^t\left\{\left[-k_{3C}(s)\frac{d^2}{dx^2}+k_{1C}(s)\right]\tau_{xy1}(x,s)+k_{2C}(s)\tau_{xy2}(x,s)+k_{8C}(s)V_1(x,s)+k_{9C}(s)V_3(x,s)\right\}ds=0 \tag{27}$$

$$k_{2E}(t)\tau_{xy1}(x,t)+\left[k_{7E}(t)\frac{d^4}{dx^4}-k_{5E}(t)\frac{d^2}{dx^2}+k_{4E}(t)\right]\tau_{xy2}(x,t)+k_{9E}(t)V_1(x,t)+k_{10E}(t)V_3(x,t)+\int_0^t\left\{k_{2C}(s)\tau_{xy1}(x,s)+\left[-k_{5C}(s)\frac{d^2}{dx^2}+k_{4C}(s)\right]\tau_{xy2}(x,s)+k_{9C}(t)V_1(x,s)+k_{10C}(s)V_3(x,s)\right\}ds=0 \tag{28}$$

It can be seen that the interfacial transverse shear forces and shear stresses are coupled; the other required equations and boundary conditions must be derived from compatibility of vertical deformations as discussed below.

3.4. Compatibility of vertical deformations

The time-dependent vertical deformations of the component, interlayer and substrate in the neighborhood of each interface, $w_j^m(x,t)$, consist of elastic displacements, $w_{jE}^m(x,t)$, and creep deformations, $w_{jC}^m(x,t)$:

$$w_j^m(x,t)=w_{jE}^m(x,t)+\int_0^t \dot{w}_{jC}^m(x,s)\,ds \tag{29}$$

The elastic interfacial displacements in Eq. (29) may be written as

$$w_{1E}^1(x,t)=\mu_{1E}(t)\int_{-l}^{x}V_1(\xi,t)\,d\xi+\delta_{1E}(t)\sigma_{y1}(x,t)+\frac{1}{D_{1E}(t)}\int_0^x\int_0^x M_1(\xi,t)\,d\xi\,d\xi' \tag{30}$$

$$w_{2E}^1(x,t)=\mu_{2E}(t)\int_{-l}^{x}V_2(\xi,t)\,d\xi-\delta_{2E}(t)\sigma_{y1}(x,t)+\frac{1}{D_{2E}(t)}\int_0^x\int_0^x M_2(\xi,t)\,d\xi\,d\xi' \tag{31}$$

$$w_{2E}^2(x,t)=\mu_{2E}(t)\int_{-l}^{x}V_2(\xi,t)\,d\xi+\delta_{2E}(t)\sigma_{y2}(x,t)+\frac{1}{D_{2E}(t)}\int_0^x\int_0^x M_2(\xi,t)\,d\xi\,d\xi' \tag{32}$$

$$w_{3E}^2(x,t)=\mu_{3E}(t)\int_{-l}^{x}V_3(\xi,t)\,d\xi-\delta_{3E}(t)\sigma_{y2}(x,t)+\frac{1}{D_{3E}(t)}\int_0^x\int_0^x M_3(\xi,t)\,d\xi\,d\xi' \tag{33}$$

where $\mu_{jE}(t)$ and $\delta_{jE}(t)$ are the transverse and through-thickness compliances, respectively, of the jth layer against elastic deformations as defined in Ghorbani and Spelt (2005) for both plane stress and plane strain conditions. In Eqs. (30)–(33), the first terms are transverse elastic deflections caused by transverse shear loads, the second terms are the local elastic displacement due to the peel stresses, and the third terms are the elastic flexural deformations.

Similarly, the rate of interfacial creep deflections in Eq. (29) can be defined as

$$\dot{w}_{1C}^1(x,t)=\mu_{1C}(t)\int_{-l}^{x}V_1(\xi,t)\,d\xi+\delta_{1C}(t)\sigma_{y1}(x,t)+\frac{1}{D_{1C}(t)}\int_0^x\int_0^x M_1(\xi,t)\,d\xi\,d\xi' \tag{34}$$

$$\dot{w}_{2C}^1(x,t)=\mu_{2C}(t)\int_{-l}^{x}V_2(\xi,t)\,d\xi-\delta_{2C}(t)\sigma_{y1}(x,t)+\frac{1}{D_{2C}(t)}\int_0^x\int_0^x M_2(\xi,t)\,d\xi\,d\xi' \tag{35}$$

$$\dot{w}^2_{2C}(x,t) = \mu_{2C}(t)\int_{-l}^{x} V_2(\xi,t)\,\mathrm{d}\xi + \delta_{2C}(t)\sigma_{y2}(x,t) + \frac{1}{D_{2C}(t)}\int_0^x\int_0^x M_2(\xi,t)\,\mathrm{d}\xi\,\mathrm{d}\xi' \tag{36}$$

$$\dot{w}^2_{3C}(x,t) = \mu_{3C}(t)\int_{-l}^{x} V_3(\xi,t)\,\mathrm{d}\xi - \delta_{3C}(t)\sigma_{y2}(x,t) + \frac{1}{D_{3C}(t)}\int_0^x\int_0^x M_3(\xi,t)\,\mathrm{d}\xi\,\mathrm{d}\xi' \tag{37}$$

where $\mu_{jC}(t)$ and $\delta_{jC}(t)$ are the transverse and the through-thickness compliances, respectively, of the jth layer against creep deformations. These compliances are derived in Appendix B for both plane stress and plane strain conditions. In Eqs. (34)–(37), the first terms are transverse creep deflections caused by $V_j(x,t)$, the second terms are local creep displacement due to the peel stresses, and the third terms are the creep flexural deformations.

Substituting for the bending moments, using compatibility of the vertical deflections at each interface (i.e. $w^1_1(x,t) = w^1_2(x,t)$ and $w^2_2(x,t) = w^2_3(x,t)$), and differentiating twice leads to the following system of coupled time-dependent integro-differential equations:

$$\begin{aligned}
&k_{8E}(t)T_1(x,t) - k_{9E}(t)T_3(x,t) + \Delta_{1E}(t)V'_1(x,t) + \Delta_{2E}(t)V'_3(x,t) - \Delta_{3E}(t)V'''_1(x,t) - \Delta_{6E}(t)\int_{-l}^{x} V_1(\xi,t)\,\mathrm{d}\xi\\
&- \Delta_{7E}(t)\int_{-l}^{x} V_3(\xi,t)\,\mathrm{d}\xi + \int_0^t\Big[k_{8C}(s)T_1(x,s) - k_{9C}(s)T_3(x,s) + \Delta_{1C}(s)V'_1(x,s) + \Delta_{2C}(s)V'_3(x,s)\\
&- \Delta_{3C}(s)V'''_1(x,s) - \Delta_{6C}(s)\int_{-l}^{x} V_1(\xi,s)\,\mathrm{d}\xi - \Delta_{7C}(s)\int_{-l}^{x} V_3(\xi,s)\,\mathrm{d}\xi\Big]\,\mathrm{d}s = 0
\end{aligned} \tag{38}$$

$$\begin{aligned}
&k_{9E}(t)T_1(x,t) - k_{10E}(t)T_3(x,t) + \Delta_{2E}(t)V'_1(x,t) + \Delta_{4E}(t)V'_3(x,t) - \Delta_{5E}(t)V'''_3(x,t) - \Delta_{7E}(t)\int_{-l}^{x} V_1(\xi,t)\,\mathrm{d}\xi\\
&- \Delta_{8E}(t)\int_{-l}^{x} V_3(\xi,t)\,\mathrm{d}\xi + \int_0^t\Big[k_{9C}(s)T_1(x,s) - k_{10C}(s)T_3(x,s) + \Delta_{2C}(s)V'_1(x,s) + \Delta_{4C}(s)V'_3(x,s)\\
&- \Delta_{5C}(s)V'''_3(x,s) - \Delta_{7C}(s)\int_{-l}^{x} V_1(\xi,s)\,\mathrm{d}\xi - \Delta_{8C}(s)\int_{-l}^{x} V_3(\xi,s)\,\mathrm{d}\xi\Big]\,\mathrm{d}s = 0
\end{aligned} \tag{39}$$

where the elastic stiffnesses Δ_{1E}–Δ_{8E} are given in Ghorbani and Spelt (2005). The creep compliances Δ_{1C}–Δ_{8C} are exactly the same as the corresponding elastic compliances except that $E_j(t)$ is replaced by $\beta_j(t)$ and v_j by 0.5. Note that $\sigma_{y1}(x,t)$ and $\sigma_{y2}(x,t)$ in Eqs. (34)–(37) were replaced by $-V'_1(x,t)$ and $V'_3(x,t)$, respectively. Note also that the assembly is not constrained in y-direction and neighboring layers at each interface experience the same thermal expansion. Therefore, the thermal expansion terms would have canceled each other in the compatibility requirements had they been taken into account in Eq. (29). Finally, another differentiation of Eqs. (38) and (39) gives:

$$\begin{aligned}
&k_{8E}(t)\tau_{xy1}(x,t) + k_{9E}(t)\tau_{xy2}(x,t) + \left[\Delta_{3E}(t)\frac{\mathrm{d}^4}{\mathrm{d}x^4} - \Delta_{1E}(t)\frac{\mathrm{d}^2}{\mathrm{d}x^2} + \Delta_{6E}(t)\right]V_1(x,t)\\
&+ \left[-\Delta_{2E}(t)\frac{\mathrm{d}^2}{\mathrm{d}x^2} + \Delta_{7E}(t)\right]V_3(x,t) + \int_0^t\Bigg\{k_{8C}(s)\tau_{xy1}(x,s) + k_{9C}(s)\tau_{xy2}(x,s)\\
&+ \left[\Delta_{3C}(s)\frac{\mathrm{d}^4}{\mathrm{d}x^4} - \Delta_{1C}(s)\frac{\mathrm{d}^2}{\mathrm{d}x^2} + \Delta_{6C}(s)\right]V_1(x,s) + \left[-\Delta_{2C}(s)\frac{\mathrm{d}^2}{\mathrm{d}x^2} + \Delta_{7C}(s)\right]V_3(x,s)\Bigg\}\,\mathrm{d}s = 0
\end{aligned} \tag{40}$$

$$\begin{aligned}
&k_{9E}(t)\tau_{xy1}(x,t) + k_{10E}(t)\tau_{xy2}(x,t) + \left[-\Delta_{2E}(t)\frac{\mathrm{d}^2}{\mathrm{d}x^2} + \Delta_{7E}(t)\right]V_1(x,t)\\
&+ \left[\Delta_{5E}(t)\frac{\mathrm{d}^4}{\mathrm{d}x^4} - \Delta_{4E}(t)\frac{\mathrm{d}^2}{\mathrm{d}x^2} + \Delta_{8E}(t)\right]V_3(x,t) + \int_0^t\Bigg\{k_{9C}(s)\tau_{xy1}(x,s) + k_{10C}(s)\tau_{xy2}(x,s)\\
&+ \left[-\Delta_{2C}(s)\frac{\mathrm{d}^2}{\mathrm{d}x^2} + \Delta_{7C}(s)\right]V_1(x,s) + \left[\Delta_{5C}(s)\frac{\mathrm{d}^4}{\mathrm{d}x^4} - \Delta_{4C}(s)\frac{\mathrm{d}^2}{\mathrm{d}x^2} + \Delta_{8C}(s)\right]V_3(x,s)\Bigg\}\,\mathrm{d}s = 0
\end{aligned} \tag{41}$$

From Eqs. (27), (28), (40) and (41), it is evident that the loading history will affect the accumulated creep deformations and the current interfacial stresses and strains.

3.5. Boundary conditions

The governing equations (27), (28), (40) and (41) represent a boundary value problem (BVP) with respect to x and an initial value problem with respect to time. Consequently, 16 BVP and four initial values are needed. The following eight BVP conditions are evident:

$$\tau_{xy1}(\pm l,t)=\tau_{xy2}(\pm l,t)=V_1(\pm l,t)=V_3(\pm l,t)=0 \tag{42}$$

Additionally, it is assumed that the assembly is free of residual stresses at the onset of loading, i.e. $t=0$, so that the following four initial values are applicable:

$$\tau_{xy1}(x,0)=\tau_{xy2}(x,0)=V_1(x,0)=V_3(x,0)=0 \tag{43}$$

Recalling Eq. (15), the remaining eight BVP conditions can also be obtained from Eqs. (25), (26), (38) and (39):

$$-k_{3E}(t)\tau'_{xy1}(\pm l,t)+k_{6E}(t)\tau'''_{xy1}(\pm l,t)-\int_0^t k_{3C}(s)\tau'_{xy1}(\pm l,s)\,\mathrm{d}s=[\alpha_1^*(t)-\alpha_2^*(t)]\Delta\theta(t) \tag{44}$$

$$-k_{5E}(t)\tau'_{xy2}(\pm l,t)+k_{7E}(t)\tau'''_{xy2}(\pm l,t)-\int_0^t k_{5C}(s)\tau'_{xy2}(\pm l,s)\,\mathrm{d}s=[\alpha_2^*(t)-\alpha_3^*(t)]\Delta\theta(t) \tag{45}$$

$$\begin{aligned}&\Delta_{1E}(t)V'_1(\pm l,t)+\Delta_{2E}(t)V'_3(\pm l,t)-\Delta_{3E}(t)V'''_1(\pm l,t)+\int_0^t[\Delta_{1C}(s)V'_1(\pm l,s)+\Delta_{2C}(s)V'_3(\pm l,s)\\&\quad-\Delta_{3C}(s)V'''_1(\pm l,s)]\,\mathrm{d}s=0\end{aligned} \tag{46}$$

$$\begin{aligned}&\Delta_{2E}(t)V'_1(\pm l,t)+\Delta_{4E}(t)V'_3(\pm l,t)-\Delta_{5E}(t)V'''_3(\pm l,t)+\int_0^t[\Delta_{2C}(s)V'_1(\pm l,s)+\Delta_{4C}(s)V'_3(\pm l,s)\\&\quad-\Delta_{5C}(s)V'_3(\pm l,s)]\,\mathrm{d}s=0\end{aligned} \tag{47}$$

The last four boundary conditions suggest that the creep deformation may also affect the stress and strain distribution at the free edges of interfaces.

These 16 boundary and four initial conditions together with the Eqs. (27), (28), (40) and (41) define the interfacial stresses in a trilayer assembly under time-dependent thermal loading with elasto-creep deformation. Note that once the transverse shear forces are determined, peel stresses $\sigma_{y1}(x,t)$ and $\sigma_{y2}(x,t)$ can be calculated from $-V'_1(x,t)$ and $V'_3(x,t)$, respectively.

3.6. Other stress and strain components

Upon finding the interfacial shear and peel stress distributions in an incremental manner with respect to time, as discussed in Section 4 below, the other components of stress and strain can be defined in the post-processing step for each time interval.

First, the axial forces $T_j(x,t)$ and bending moments $M_j(x,t)$ can be determined using Eqs. (5)–(8) and (12)–(14). The axial stresses $\sigma^m_{xj}(x,t)$ in each layer at each interface for both plane stress and plane strain conditions may then be approximated by

$$\sigma^m_{xj}(x,t)=\frac{T_j(x,t)}{h_j}\mp\frac{6M_j(x,t)}{h_j^2} \tag{48}$$

where $+$ and $-$ signs refer to the lower and upper interfaces of each layer, respectively.

The total normal and shear strains at each interface may encompass thermal, elastic and instantaneous creep components as

$$\varepsilon^m_{xj}(x,t)=\varepsilon_j^{\mathrm{th}}(t)+\varepsilon^m_{xjE}(x,t)+\varepsilon^m_{xjC}(x,t) \tag{49}$$

$$\varepsilon^m_{yj}(x,t)=\varepsilon_j^{\mathrm{th}}(t)+\varepsilon^m_{yjE}(x,t)+\varepsilon^m_{yjC}(x,t) \tag{50}$$

$$\varepsilon^m_{zj}(x,t) = \varepsilon^{\text{th}}_j(t) + \varepsilon^m_{zj\text{E}}(x,t) + \varepsilon^m_{zj\text{C}}(x,t) \tag{51}$$

$$\varepsilon^m_{xyj}(x,t) = \varepsilon^m_{xyj\text{E}}(x,t) + \varepsilon^m_{xyj\text{C}}(x,t) \tag{52}$$

where the thermal strain is equal to $\alpha_j(t)\Delta\theta(t)$, elastic strains can be found through Hook's law, and the creep strains can be obtained by integration of the creep law in Eqs. (1)–(4). However, the elastic and creep strain components under plane strain conditions require identification of the out-of-plane stresses $\sigma^m_{zj}(x,t)$. In order to define these stresses one must realize that even though the total strain in the z-direction is zero under plane strain conditions, its thermal, elastic, and creep components do exist. In other words, the component strains in Eq. (51) interact with each other so that the total z-strain vanishes. Substituting for the strain components in Eq. (51), and setting the total z-strain to be zero yields the following supplementary equation which defines the $\sigma^m_{zj}(x,t)$:

$$\alpha_j(t)\Delta\theta(t) + \frac{1}{E_j(t)}\left[\sigma^m_{zj}(x,t) - v_j(\sigma^m_{xj}(x,t) + \sigma_{ym}(x,t))\right] + \int_0^t \frac{1}{\beta_j(s)}\left[\sigma^m_{zj}(x,s) - 0.5(\sigma^m_{xj}(x,s) + \sigma_{ym}(x,s))\right] \mathrm{d}s = 0 \tag{53}$$

Having specified the stress components, interfacial von Mises stresses $S^m_j(x,t)$ may be defined as

$$S^m_j(x,t) = \{[\sigma^m_{xj}(x,t) - \sigma_{ym}(x,t)]^2 + [\sigma^m_{xj}(x,t) - \sigma^m_{zj}(x,t)]^2 + [\sigma_{ym}(x,t) - \sigma^m_{zj}(x,t)]^2 + 6\tau_{xym}(x,t)^2\}^{0.5}/\sqrt{2} \tag{54}$$

Note that the $\sigma^m_{zj}(x,t)$ are zero under the plane stress condition. The von Mises elastic strains are related to the von Mises stress through

$$\varepsilon^m_{j\text{VME}}(x,t) = \frac{S^m_j(x,t)}{E_j(t)} \tag{55}$$

Such a relationship, however, does not exist between the von Mises stress and von Mises creep strain. The latter may be computed as (ANSYS 8.0, 2003)

$$\varepsilon^m_{j\text{VMC}}(x,t) = \frac{2}{3}\left\{0.5[(\varepsilon^m_{\text{I}j\text{C}}(x,t) - \varepsilon^m_{\text{II}j\text{C}}(x,t))^2 + (\varepsilon^m_{\text{I}j\text{C}}(x,t) - \varepsilon^m_{\text{III}j\text{C}}(x,t))^2 + (\varepsilon^m_{\text{II}j\text{C}}(x,t) - \varepsilon^m_{\text{III}j\text{C}}(x,t))^2]\right\}^{0.5} \tag{56}$$

where $\varepsilon^m_{\text{I}j\text{C}}(x,t)$, $\varepsilon^m_{\text{II}j\text{C}}(x,t)$, and $\varepsilon^m_{\text{III}j\text{C}}(x,t)$ are the principal creep strains. Since the out-of-plane shear creep strains are neglected, the principal creep strains may be determined as

$$\varepsilon^m_{\text{I}j\text{C}}(x,t) = \varepsilon^m_{zj\text{C}}(x,t) \tag{57}$$

$$\varepsilon^m_{\text{II}j\text{C}}(x,t), \varepsilon^m_{\text{III}j\text{C}}(x,t) = 0.5[(\varepsilon^m_{xj\text{C}}(x,t) + \varepsilon^m_{yj\text{C}}(x,t)) \pm \sqrt{(\varepsilon^m_{xj\text{C}}(x,t) + \varepsilon^m_{yj\text{C}}(x,t))^2 - 4(\varepsilon^m_{xj\text{C}}(x,t)\varepsilon^m_{yj\text{C}}(x,t) - 0.25(\varepsilon^m_{xyj\text{C}}(x,t))^2)}] \tag{58}$$

It is noted that the creep strains in Eq. (49)–(52) and (56) are all instantaneous values since the stress components can be either positive or negative. In order to reflect the irreversible damage accumulation due to creep deformation, the "accumulated creep strain", $\varepsilon^m_{j\text{AC}}(x,t)$, is defined as

$$\varepsilon^m_{j\text{AC}}(x,t) = \int_0^t \frac{S^m_j(x,s)}{\beta_j(s)}\,\mathrm{d}s \tag{59}$$

This creep strain is particularly useful in cyclic applications with load reversal since it always increases, regardless of whether the load is increasing or decreasing. The accumulated creep strain in ANYSYS 8.0 (2003) is called the "equivalent creep strain" and is the same as that in Eq. (59).

3.7. Creep strain energy density

Creep strain energy density at the interfacial points can be found as (ANSYS 8.0, 2003)

$$W^m_{j\text{C}}(x,t) = \int_0^{\varepsilon^m_{j\text{AC}}(x,t)} S^m_j(x,t)\,\mathrm{d}\varepsilon^m_{j\text{AC}}(x,t) \tag{60}$$

Note that von Mises creep strain (Eq. (56)) was not used in Eq. (60) as it may decrease during the stress reversal in cyclic applications (Fig. 6), resulting negative creep strain energy density which is unrealistic since the creep strain energy always increases (i.e. non-recoverable energy). For monotonic loading conditions, however, use of von Mises and accumulated creep strains results in the same predictions for creep strain energy density. The accumulated strain energy density (or strain energy dissipation) may be used as a measure of creep damage evolution and increases monotonically during thermal cycling.

4. Solution method

A closed-form solution for Eqs. (27), (28), (40)–(47), if available, would lead to non-linear (eigenvalue) expressions that would have to be solved numerically. The usual procedure involves parameterization of the differential equations followed by an appropriate shooting or relaxation technique or a combination of both. To account for the time-dependent nature of the partial differential equations, Dirichlet's series expansion (e.g. Bruno et al., 1999) or Hermite polynomials may be required.

A more straightforward and flexible approach is to use a first-order finite difference procedure in which the interfacial regions are discretized into n divisions (n even) such that $i = 1$ on the left side and $i = n$ on the right (Ghorbani and Spelt, 2005). The first four derivatives of $\tau_{xym}(x,t)$ with respect to x are then approximated by

$$i \leqslant \frac{n}{2}: \quad \tau_{xym}^{(r)}(i,s) = \frac{\tau_{xym}^{(r-1)}(i+1,s) - \tau_{xym}^{(r-1)}(i,s)}{p^r} \tag{61}$$

$$i \geqslant \frac{n}{2}: \quad \tau_{xym}^{(r)}(i,s) = \frac{\tau_{xym}^{(r-1)}(i,s) - \tau_{xym}^{(r-1)}(i-1,s)}{p^r} \tag{62}$$

where the order of the derivative is $r = 1$–4, and $p = L/n$ is the pitch between the interfacial divisions. Similar expressions can be written for the derivatives of $V_j(x,t)$.

The time is also divided into t one-second increments (t being an integer) such that $s = 0$ for time zero and $s = t$ for the end of loading. The time integrals can then be expanded into two terms; a summation representing the sum of the previous values of time-related creep parameters (i.e. displacements and their derivatives, strain, and strain energy) and a current value. For example,

$$\int_0^t k_{2C}(s)\tau_{xy1}(x,s)\,\mathrm{d}s = k_{2C}(t)\tau_{xy1}(x,t) + \sum_{s=0}^{t-1} k_{2C}(s)\tau_{xy1}(x,s) \tag{63}$$

Note that the initial values ($s = 0$) of forces, stresses, strains, and strain energies are zero; therefore, the summation of these parameters is effective from $s = 1$.

Using the above definitions, the governing differential equations and the relevant boundary conditions may be discretized. At each time increment, first the time-dependent thermomechanical parameters (i.e. $\beta_j(s)$ $E_j(s)$, and stiffnesses) are evaluated. Then the system of linear equations is solved for the current values of $\tau_{xy1}(i,s)$, $\tau_{xy1}(i,s)$, $V_1(i,s)$, and $V_3(i,s)$. Forces, moments, and their derivatives as well as other components of stress and strain, and creep strain energy density may then be computed as a post-processing step for this increment of load (time). The current values of creep strain and creep strain energy density will then be added to the previously accumulated ones serving as the new accumulated values for the next time increment.

5. Model evaluation

5.1. Test cases

For illustrative purposes, numerical results are presented for four microelectronic trilayers given in Table 1. In all examples, a resistor component (silicon chip) is attached to a printed circuit board substrate (FR-4 glass–fiber reinforced epoxy laminate) using either a tin–lead (SnPb) or lead-free solder (tin–silver–copper, SAC). It is assumed that the elastic modulus of the solder is temperature dependent and that only the solder layer undergoes creep deformation. In general, solders experience large creep deformation due to their

relatively low melting point. In order to assess accuracy and generality of the present model, aspect ratio, solder properties, and the creep constitutive law of the solder layer are varied among these four trilayer examples.

Examples 1 and 2 are relatively short trilayers and differ only in the choice of the creep model for lead-free solder: the second uses the Garofalo hyperbolic sign steady-state creep model (Qi et al., 2004; ANSYS 8.0, 2003) and the first employs a linear viscous creep model (i.e. Norton–Arrhenius creep law in ANSYS with unit power for stress) based on a linear regression of the Garofalo model from 0 to 57 MPa. The third example is similar to the first, but with the eutectic SnPb solder as the interlayer, modeled with the Garofalo creep law. The fourth example is the same as the second, but with a smaller aspect ratio (i.e. a relatively long trilayer).

The governing equations in the present model were solved for the interfacial shear stresses and transverse shear forces under plane strain condition along the x–y plane of symmetry at $z = 0$ (Fig. 1) using the Compaq Visual FORTRAN 6.6 (2000) International Mathematical and Statistical Library (IMSL) subroutine DLSARG. This subroutine solves a real system of linear equations with double precision iterative refinement. It was found that the number of elements (n) should be greater than 100 for the short trilayers and 400 for the long trilayer in order to attain solutions that are relatively independent of n.

The predictions of the present model were compared with those of two finite element models built in ANSYS 8.0 (2003): one for the short trilayers of Examples 1–3 and the other for the long trilayer in Example 4. The assemblies were meshed using PLANE183 elements having 8 nodes and 16 degrees of freedom, and symmetry boundary conditions were applied to the left end of the models. For both models, progressive refinements in mesh densities were examined for the lower and upper interfaces. Regardless of the element size or shape, all of these FE models displayed a stress distribution in the interfacial region near the free ends of interfaces ($|x| \geqslant 0.8l$ for short trilayer and $|x| \geqslant 0.9l$ for long trilayer) that was highly sensitive to the mesh density. Away from these end regions, the FE stress distribution was insensitive to mesh density. This behavior of the FE model is similar to that reported by many researchers; e.g. Glaser (1990), Basaran and Zhao (2001), and Ghorbani and Spelt (2005).

The interfacial FE stresses were obtained from the element results; not the nodal results which are the average of the stresses in the adjacent layers wherever there is a material discontinuity. This is because the shear and peel stresses are the same for adjacent materials across each interface (Fig. 1), whereas the interfacial axial, out-of-plane, and von Mises stresses are discontinuous from one layer to the other, depending strongly on the materials bonding the interface (Eqs. (48), (53), (59)).

A uniform cyclic temperature change (Fig. 2) with 5 min lower and upper dwells at zero and 100 °C, respectively, and with identical heating and cooling phases of 95 °C/min was applied to the four examples. The

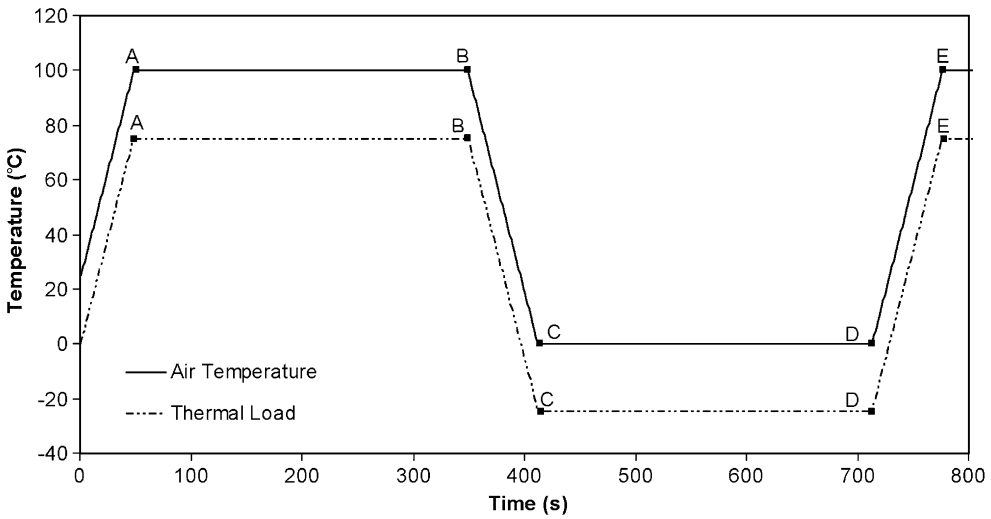

Fig. 2. Thermal cycling profile used in all examples. Path A–B–C–D–E represents one cycle. Thermal load defined relative to the stress-free temperature of 25 °C.

actual thermal cycling load was 25 °C less than the air temperature as the assemblies were assumed to be stress-free at room temperature.

The present model was executed with $n = 200$ (3.8 μm) and $n = 500$ (7.6 μm) for short and long trilayers, respectively. The FE model for the short trilayer had 3328 elements (i.e. element size of 8.3×8.3 μm near the free ends) while that for the long trilayer of Example 4 had 6357 elements (i.e. element size of 13.8×13.2 μm near the free ends).

5.2. Choice of shear stiffness parameter

As mentioned above in the context of Eqs. (17)–(20), the present model can satisfy the zero shear stress condition at the free ends of the trilayer by incorporating the second derivative of shear stress in the horizontal displacement at interfacial points (Ghorbani and Spelt, 2005). With the shear stiffness parameter $d_j \leqslant h_j^2/1000\pi^2$, the maximum shear stresses lie in the immediate vicinity of the free edges ($x = \pm l$). As d_j approaches zero, the location of the maximum shear stresses moves closer to the ends; however, the other stress components do not change.

Using the present elasto-creep analytical model, it was noticed for all four examples with $d_j = h_j^2/1000\pi^2$ that during the first heating phase (from time zero to the point A in Fig. 2) the shear stress distributions in the short and long trilayers were qualitatively the same as those observed in the elastic analysis of Ghorbani and Spelt (2005). In the early stage of the first dwell, however, the relatively large strains produced by creep caused the location of the interfacial shear stress maxima to shift toward the free ends of the trilayer. After only a few seconds of dwell at the high temperature, the shear stress distribution approximated that for $d_j = 0$, reaching a finite maxima as seen in Fig. 3a.

This gradual movement of the shear stress peak toward the free ends, while other stress components were left intact, ultimately resulted in a mathematical instability in the numerical solution; i.e. the number of assigned divisions (n) could not be made large enough to capture the steepening shear stress gradient at the free ends required to meet the zero shear stress boundary condition. A similar situation was observed by Lee and Kim (2004) in the viscoelastic analysis of interfacial stresses between a viscoelastic thin film and an elastic substrate.

The shear parameters d_j are therefore suggested to be effectively zero for inelastic analyses. Although this simplification results in violation of the zero shear stress boundary conditions, the predictions are believed to be accurate except in the vanishingly small distance from $x = \pm l$ (Ghorbani and Spelt, 2005). This is confirmed by the experimental evidence of Mirman (1991), Wang and Lin (2003), and Wen and Basaran (2004), none of whom could capture the zero shear stress or very steep shear stress gradient close to the free ends of interfaces.

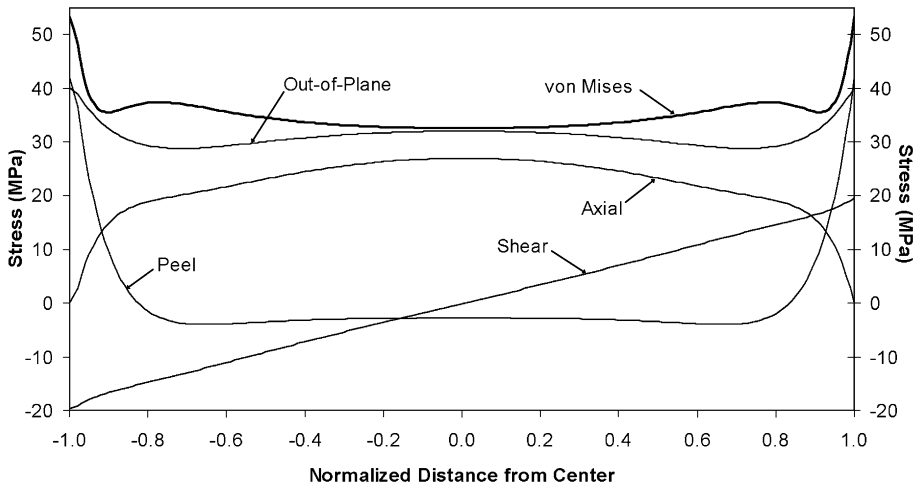

Fig. 3a. Stress distribution at upper interface in short SAC solder joint of Example 1 (linear creep model) at 3625 s (i.e. end of lower dwell in fifth cycle).

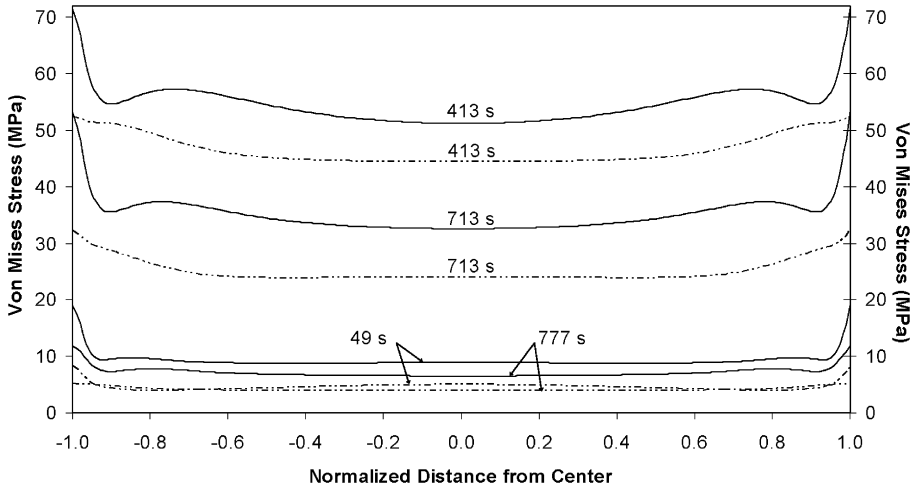

Fig. 3b. Interfacial von Mises stresses in short SAC solder joint of Example 1 (linear creep model) at times A, C, D, and E in Fig. 2. Dashed lines are those of the lower interface and solid lines are those of the upper interface.

Therefore, the shear stress maxima must indeed be extremely close to the free edges, particularly with creep deformation. Note that the simplifying assumption of $d_j = 0$ does not alter any compatibility requirements or other boundary conditions, and that all stress components except for the von Mises stress are unchanged. In particular, it does not produce any stress singularity as is the case for elasticity solutions with $d_j = 0$ (Yin, 1991; Ghorbani and Spelt, 2005).

5.3. Adaptation of non-linear creep model

The linear creep model of Example 1 contains a creep viscosity that is constant over the trilayer, being only a function of temperature (Eqs. (1)–(4) and Table 1) and, therefore, independent of stress.

The non-linear creep model (Eq. (5) and Table 1) contains a creep viscosity that is a function of both temperature and stress, and hence varies along the trilayer. An exact solution would make the present model formulation enormously complicated since the creep viscosity could no longer be treated as a constant in differentiations with respect to x in Sections 3.3 and 3.4 above. In order to avoid such complications, the von Mises stress of the interfacial point for which the results are to be retrieved is used to define the uniform creep viscosity for the entire trilayer at each time interval (temperature). It was hypothesized that this approximation would produce acceptably small errors because the von Mises stress distribution throughout the layers was found to be relatively constant away from the free ends (Fig. 3b). Close to the ends, where the von Mises stress increases, the approximation will conservatively overestimate the amount of creep over the entire trilayer. The validity of this approximate treatment of non-linear creep will become evident in the results of Examples 2–4.

6. Results and discussion

Figs. 3a and 3b show the typical time-dependent distribution of interfacial stresses in Example 1 predicted by the present elasto-creep model (with $d_j = 0$). Fig. 3a illustrates the distribution of stress components across the upper interface at the end of lower dwell of fifth thermal cycle. Fig. 3b depicts the variation of von Mises stresses along both the upper and lower interfaces at different stages of the first thermal cycle.

Figs. 3a and 3b illustrate certain common features of interfacial stresses at both the upper and lower interfaces of the solder layer for all four examples:

(1) Higher stresses and strains are predicted at the upper interface than at the lower interface (Fig. 3b). This is related to the greater CTE and rigidity mismatch between the solder and the silicon chip component at the upper interface than that between the solder and the FR-4 substrate at the lower interface.

(2) The out-of-plane stresses have symmetric distributions and usually have the largest magnitude among the stress components (Fig. 3a).
(3) Axial stresses have symmetric distributions and are zero at the free ends. Near the middle of the assembly, they are usually larger in magnitude than either the shear or peel stresses (Fig. 3a), particularly for the elongated trilayer in Example 4.
(4) Shear stresses have antisymmetric distributions, are zero at $x = 0$ and often maximum at the free edges (Fig. 3a). A gradual increase in the shear stress from the middle to the free ends is typical for short assemblies (Examples 1–3), whereas a sharp increase close to the free ends is typical in the elongated trilayer (Example 4). Note that the magnitude of the shear stress at each interface is the slope of the axial stress curve.
(5) Peel stresses have symmetric distributions and are minimum in the middle of the assembly and usually maximum at the free edges (Fig. 3a). Close to the free ends, peel stresses show both negative and positive signs in order to be self-equilibrating over each half of the interface. The magnitude of peel stresses at the free ends is often greater than that of the shear stresses. The peel stress at each interface is equal to the slope of the transverse shear force distribution, which is antisymmetric.
6) The von Mises stresses have symmetric distributions and are relatively constant along the interfaces except very near the free ends where they usually reach their maximum (Figs. 3a and 3b). However, for short periods of time during the early stages of thermal dwells, particularly the upper dwell, the location of the maximum of von Mises stress may move to the middle of the assembly. This is because stress components have different relaxation rates. It is anticipated that cracks initiating at the ends of the joint and propagate relatively quickly due to the fairly constant magnitude of the Von-Mises stress along the interface.

These observations were supported by the results of the FE models along each interface away from the free ends. As mentioned above, the magnitudes of the FE stresses were, however, uncertain very close to the free ends due to the stress singularity (Ghorbani and Spelt, 2005). Consequently, the FE results violated the stress boundary conditions (i.e. zero shear and axial stresses at the free ends) and the peel stresses were not self-equilibrating.

Fig. 4 shows the stresses predicted by both the FE and present models at an interfacial point close to the end of the upper interface (node 179 at $x \approx 0.8l$ in Figs. 3a and 3b) in the lead-free solder layer of Example 1 during the first thermal cycle. This node was selected because it was approximately the closest node to the end of upper interface in Examples 1–3 that was not affected by the stress singularity in the FE model (i.e. it was

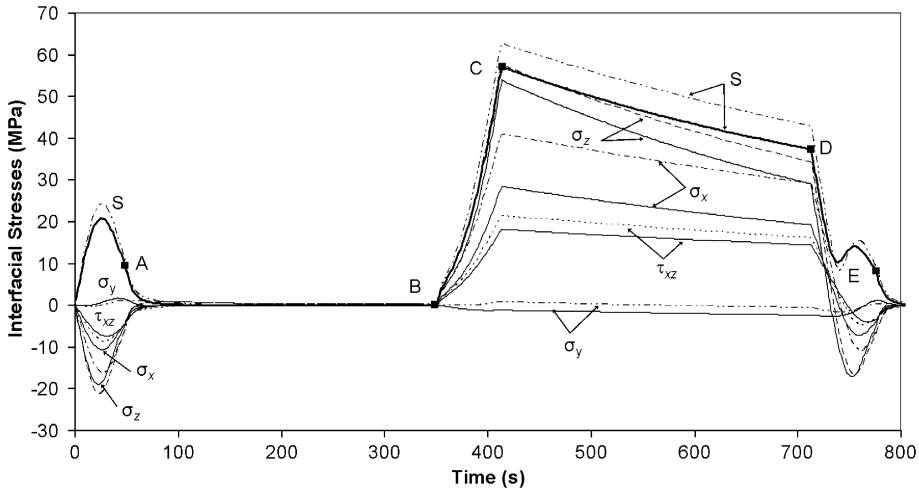

Fig. 4. Stresses at node 179 of upper interface in short SAC solder joint of Example 1 (linear creep model). Dashed lines are FE results and solid lines are those of the present model.

fairly insensitive to mesh density). Figs. 5 and 6 show the corresponding elastic and creep strains. It can be seen that the predictions of the present model closely match those of the FE model. These stresses and strains can be explained for each phase of the thermal cycle of Fig. 2 as follows:

Heating ($0 \leqslant t < 49$ s)

From time 0–25 s, when the temperature is below 65 °C, all stresses increase in magnitude almost linearly with the changing temperature (Fig. 4) since the creep is relatively small (Figs. 5 and 6). From 25 s to point A, however, the stresses decrease while the temperature is still increasing (Fig. 4), because the increasing solder creep strains (Fig. 6) cause stress relaxation thereby reducing elastic deformation across the interlayer (i.e. decreasing the elastic strains, Fig. 5).

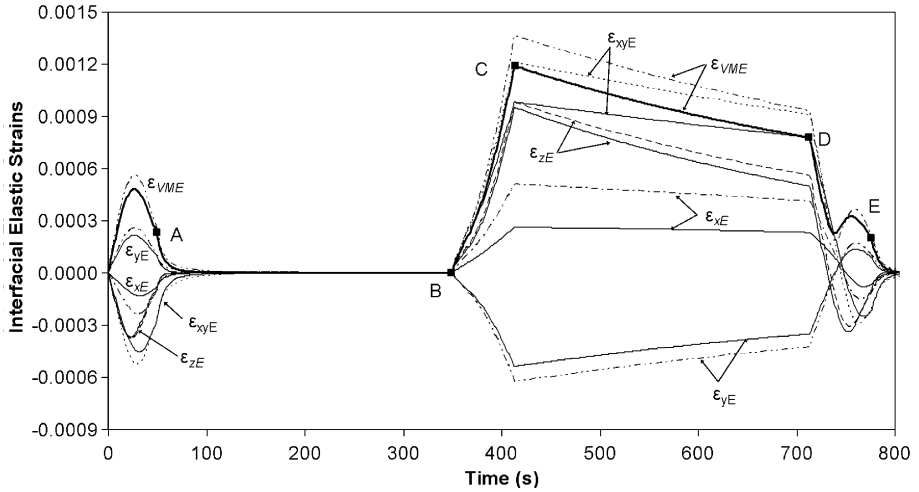

Fig. 5. Elastic strains at node 179 of upper interface in short SAC solder joint of Example 1 (linear creep model). Dashed lines are FE results and solid lines are those of the present model.

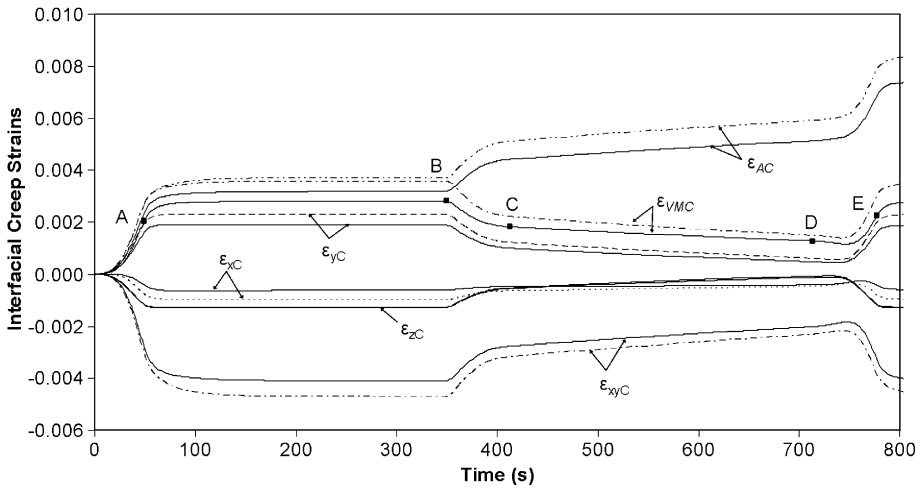

Fig. 6. Creep strains at node179 of upper interface in short SAC solder joint of Example 1 (linear creep model). Dashed lines are FE results and solid lines are those of the present model.

Upper dwell ($50 \leqslant t < 349$ s)

From A to B, when the temperature is held constant at 100 °C, stress relaxation causes the von Mises stress to decrease (Fig. 4). As expected, elastic strains also decrease and follow the same trend as the stresses (Fig. 5), whereas creep strains initially continue to increase at a high rate (Fig. 6) at this elevated temperature. Shortly beyond point A, however, the rate of creep deformation slows and stops altogether as the stresses fully relax.

Cooling ($350 \leqslant t < 413$ s)

From B to C, the stresses and elastic strains increase in magnitude as the cooling phase begins, reaching their maximum at the onset of the lower dwell at point C (Figs. 4 and 5). Note that, at room temperature (25 °C), the permanent creep deformation creates a residual von Mises stress of approximately 35 MPa (Fig. 4). The accumulated creep strain continues to increase as the stresses rise from zero, but more slowly than during the heating phase (Fig. 6), because the creep rigidity increases as the temperature decreases. Note also that the instantaneous creep strains decrease during the cooling phase due to the reversal in the sign of the stresses (Fig. 6).

Lower dwell ($414 \leqslant t < 713$ s)

Quasi-linear stress relaxation, and hence elastic strain reduction, is evident during the lower dwell from C to D; however, full stress relaxation does not occur at this low temperature because creep is less activated than that of the upper dwell (Fig. 4).

Second heating ($714 \leqslant t < 777$ s)

During the second and subsequent heating phases (D–E), the von Mises stress decreases non-monotonically (Fig. 4). This trend is due to the competing effects of stress reversal and stress relaxation. The local minimum in the von Mises stress between D and E (Fig. 4) corresponds to a reversal in the sign of the stress components a few seconds after the temperature passes room temperature, i.e. at 41 °C. Concurrently, from D to this point, the creep strains continue declining (Fig. 6). As the temperature increases beyond 41 °C, the stress components continue to increase in the negative direction, and the von Mises stress approaches a local maximum at 65 °C. As the temperature rises further, the stresses fall as creep deformation increases (Fig. 6). It is noted that the residual von Mises stress at 25 °C is dependent on the immediate thermal history, being approximately 16 MPa during the heating phase and about 35 MPa during cooling.

These patterns of stress and strain oscillation were repeated during subsequent cycles indicating a rapid stabilization of the deformation response.

Figs. 5 and 6 show that the shear stress was not necessarily the largest stress component close to the free ends, but the elastic and creep shear strain components were the largest in these regions. Away from the free ends, the shear component of elastic and creep strain decreased to zero in the middle of the assembly. Axial, peel, and out-of-plane strains were not as predictable as the shear strains because they are related to more than one stress component. In general, the out-of-plane elastic strains were among the largest elastic strains along the length of an assembly, but they were among the smallest creep strain components (Figs. 5 and 6). Axial and peel strains (both elastic and creep) were larger than the shear strains close to the middle of assembly and were moderately large elsewhere.

Figs. 7 and 8 show the interfacial von Mises stress and the accumulated strain (Eq. (59)) at node 179 on the upper interface for Examples 2 and 3 (short trilayer with SAC and SnPb solders, respectively). The two models follow very similar trends. During the upper and lower dwell periods (A–B and C–D) the FE model predicts a von Mises stress that is approximately 10% larger than that for the present model.

Comparing Figs. 7 and 4 illustrates the differences between the non-linear and linear creep laws for the same trilayer assembly. For instance, stress relaxation in the SAC solder of Example 2 with non-linear creep behavior occurs at a higher temperature (76 °C) than that of Example 1 with linear creep behavior (65 °C), thereby producing lower creep strains (Fig. 8) and larger stresses (Figs. 4 and 7) under the same thermal cycling load.

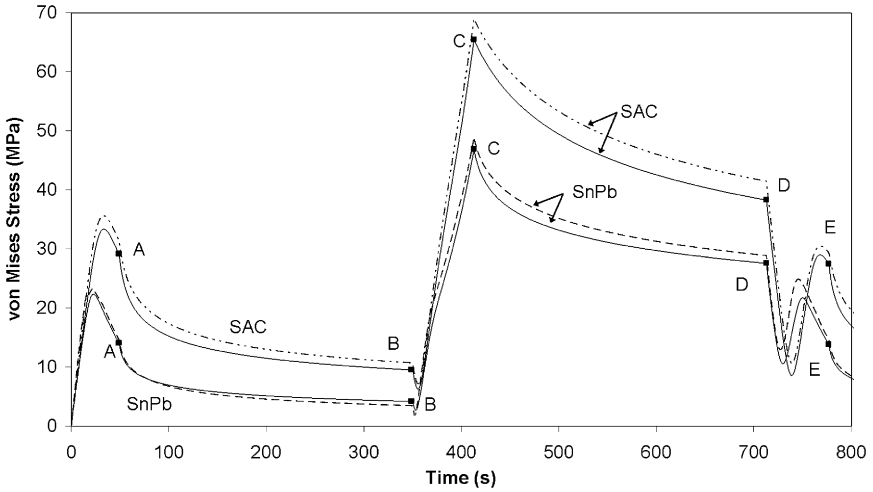

Fig. 7. Von Mises stresses at node 179 of the upper interface in Examples 2 and 3 comparing two types of solder in a short assembly (non-linear creep model). Dashed lines are FE results and solid lines are those of the present model.

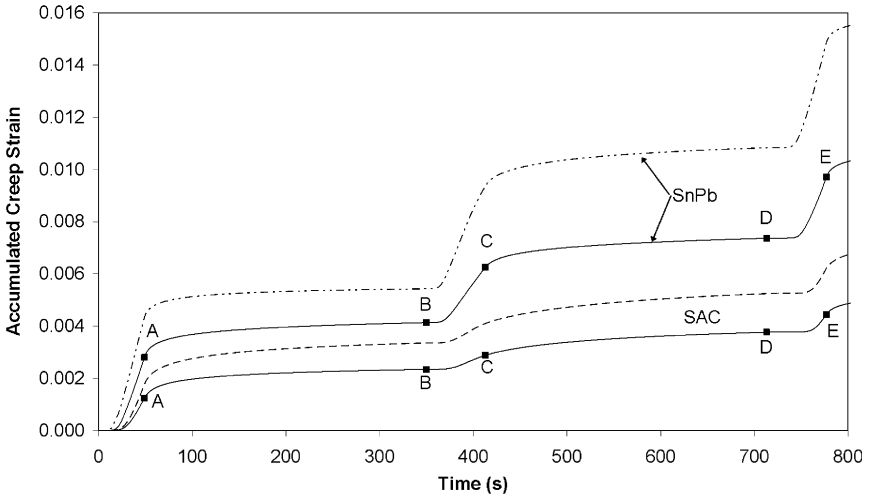

Fig. 8. Accumulated creep strains (Eq. (59)) at node 179 of the upper interface in Examples 2 and 3 comparing two types of solder in a short assembly. Dashed lines are FE results and solid lines are those of the present model.

In addition, stress relaxation during the dwell times follows a curve with the non-linear creep model (Fig. 7) and a quasi-linear trend with the linear model (Fig. 4). Finally, the linear creep model leads to the complete relaxation of stress during the high temperature dwell while this does not occur with the non-linear model.

Fig. 9a and b shows the von Mises stress versus the von Mises creep strain for node 179 of the upper interface of trilayers in Examples 1–3 during the first few thermal cycles. It is seen that the deformation-controlled stresses and strains in the isotropic elasto-linear creep material of Example 1 rapidly shakedowns (Fig. 9a) under thermal cycling conditions in the absence of plastic deformation so that the curves superimpose very closely. This behavior is consistent with the predictions of Eslami and Mahbadi (2001). Note that a ratcheting in the stress–strain hysteresis would be seen had the von Mises stress been plotted versus the accumulated creep strain. The results for the SAC and SnPb solders of Examples 2 (Fig. 9a) and 3 (Fig. 9b) with the non-linear creep model show a slightly slower stabilization than seen with the linear creep model of

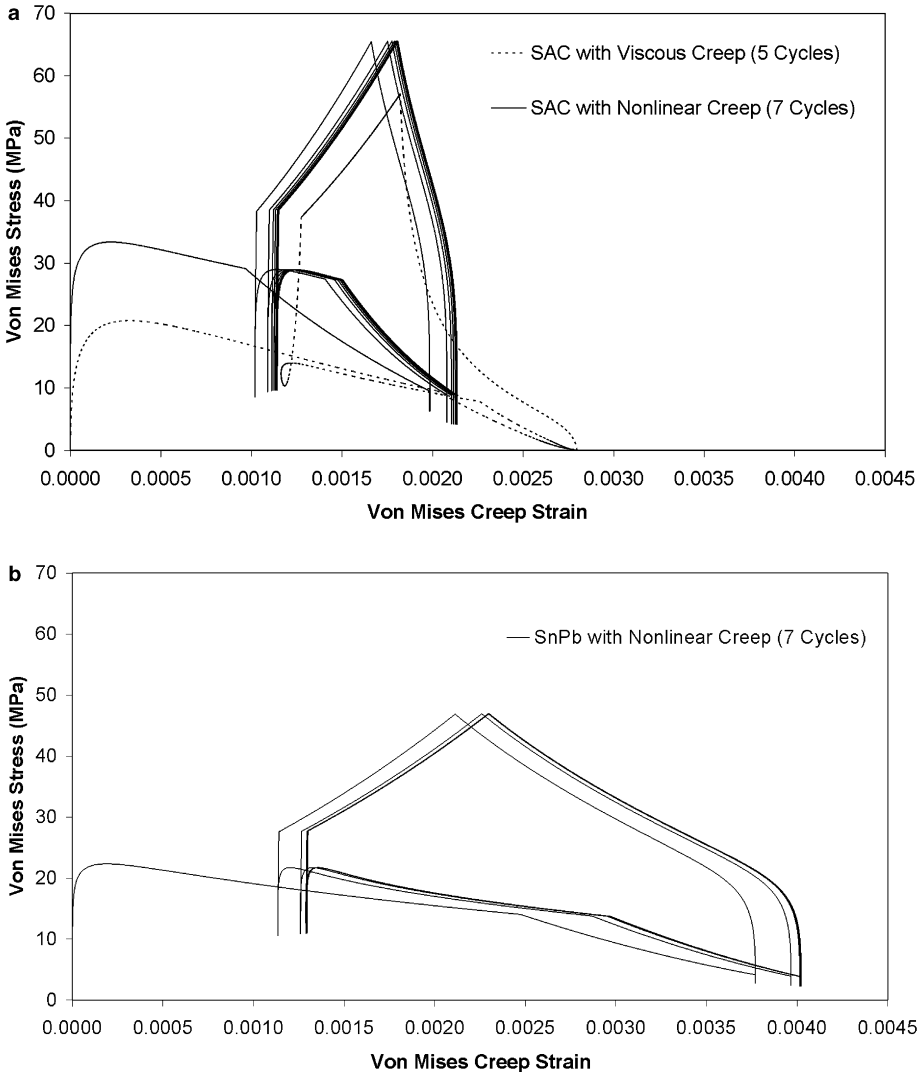

Fig. 9. Von Mises stress as a function of von Mises creep strain predicted by the present model at node 179 of the upper interface in the short solder joint of: (a) Examples 1 (shakedown under viscous creep; the 5 curves overlap) and 2 (ratcheting under nonlinear creep), (b) Example 3 (ratcheting under nonlinear creep).

Fig. 9a. As expected from its greater tendency to creep, the size of the hysteresis loop with the SnPb solder is appreciably larger than that of the SAC solder modeled with either the linear or non-linear creep laws.

In general, the FE results were very similar with those shown in Fig. 9a and b and other interfacial nodes away from the free ends. At the end regions, however, the FE results were quantitatively uncertain because of their mesh sensitivity, but they qualitatively indicated the same trend as that of the present model.

The stabilized ranges per thermal cycle of the interfacial von Mises stress, accumulated creep strain, and strain energy dissipation per cycle (area enclosed by the von Mises stress–creep strain hysteresis loop) are given in Table 2 for nodes 179 ($x \approx 0.8l$) and 200 (right free end, $x = l$) of both interfaces in Examples 1–3. These quantities are frequently used as measures of damage per cycle in thermal fatigue life models. As expected, the FE and present model both predict a higher cyclic range of stress, creep strain, and strain energy dissipation for node 179 at the upper interface than at the lower interface. In addition, the present model predicts that each of these cyclic ranges is maximum at the free ends of both interfaces, suggesting that this would be the site of crack initiation. As before, the predictions of the FE model were uncertain because of the mesh sensitivity at the free ends.

Table 2
Cyclic range of interfacial von Mises stress (ΔS), accumulated creep strain ($\Delta\varepsilon_{AC}$), and creep strain energy (ΔW_C) in Examples 1–4 as predicted by the present model (PM) and FEA

Example	L (mm)	n	Node	x/l	m	ΔS (MPa)			$\Delta\varepsilon_{AC} \times 10^3$			ΔW_C (MPa) $\times 10^2$		
						PM	FEA	% Deviation	PM	FEA	% Deviation	PM	FEA	% Deviation
1	0.76	200	179	0.8	1	49.0	42.6	15.0	3.1	2.9	6.9	4.8	3.7	29.7
					2	57.1	62.7	8.9	4.2	4.7	10.6	7.4	9.4	21.3
			200	1.0	1	52.5			3.6			5.3		
					2	71.5			6.2			13.2		
2	0.76	200	179	0.8	1	60.9	54.9	−10.9	2.1	1.6	31.2	7.2	5.0	44.0
					2	61.4	64.4	4.7	2.9	3.9	25.6	10.3	14.7	29.9
			200	1.0	1	59.0			2.2			7.4		
					2	66.2			4.8			18.7		
3	0.76	200	179	0.8	1	39.7	40.5	2.0	3.0	3.0	0.0	6.3	6.2	1.6
					2	43.1	46.9	8.1	6.7	10.5	36.2	15.9	26.8	40.7
			200	1.0	1	39.7			3.4			7.2		
					2	45.6			11.4			29.0		
4	3.8	500	475	0.9	1	52.9	51.2	−3.3	2.0	2.1	4.8	6.4	6.3	1.6
					2	57.3	59.8	4.2	3.4	3.9	12.8	11.2	13.5	17.0
			500	1.0	1	55.0			3.0			8.4		
					2	60.7			8.9			32.8		

$m = 1$ is the lower interface of the middle layer, $m = 2$ is the upper interface.

In general, the present model predictions for these stabilized ranges agree well with the FE results at node 179 (Table 2). The strain energy dissipation per cycle showed a larger discrepancy because it is sensitive to differences in either the von Mises stress or the accumulated creep strain.

Fig. 10 shows the interfacial von Mises stress and accumulated creep strain at node 475 ($x \approx 0.9l$) on the upper interface of the elongated trilayer of Example 4. This was the closest node to the free end of the upper interface that was not affected by the stress singularity in the FE model. The predictions of the two models are quite close, and are very similar to those seen in Fig. 7 for Example 2 (same solder but short trilayer). It is interesting to note that the stress singularity region in the long trilayer is limited to a smaller percentage of interfacial length (~10%) than in short trilayers (~20%) because of the differences in the interfacial shear and peel stress distributions (Ghorbani and Spelt, 2005). In other words, interfacial shear and peel stresses are zero for the majority of the interfacial length in long trilayers and rise sharply close to the free ends.

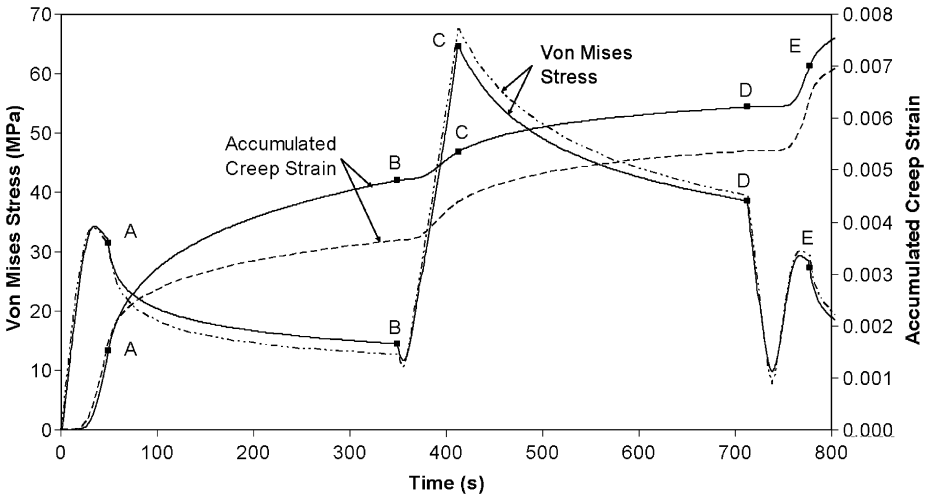

Fig. 10. Von Mises stress and accumulated creep strain at node 475 of the upper interface in the long assembly of Example 4 (SAC solder, non-linear creep model). Dashed lines are the FE results and solid lines are those of the present model.

Table 2 gives the stabilized ranges of the interfacial von Mises stress, accumulated creep strain, and the strain energy dissipation per cycle at nodes 475 and 500 (right free end) of both interfaces in Example 4. Generally, the present model predictions for these cyclic parameters agree well with those of the FEA at node 475 of both interfaces. Once again, the upper interface is more critical than the lower interface, and dissipates 1.8 times more creep strain energy per cycle than that of the same corner in the short trilayer of Example 2. This implies that more elongated assemblies will tend to increase the creep damage at the relevant free ends. As before, FE predictions were inconsistent at the free end of the trilayer because of the high degree of mesh sensitivity.

7. Conclusions

A semi-analytical 2D model has been developed for elasto-creep interfacial stresses and strains in trilayer assemblies of arbitrary aspect ratio under both constant and time varying thermal loads. The model works under both the plane stress and the plane strain conditions, can accommodate both linear (viscous) and non-linear creep constitutive laws in any of the layers, and satisfies compatibility, equilibrium, and force and stress boundary requirements. The model captures the very large shear stress gradients near the free ends in the vicinity of the maximum shear stress. It was seen that creep accumulation does not affect the magnitude of the shear stress maxima, but shifts its location progressively closer to the free ends. Consequently, it was assumed that, under creep conditions, the maximum interfacial shear stress occurs at the free ends rather than in their immediate vicinity.

Comparisons with finite element (FE) models for four examples representative of solder joints show similar trends, both qualitatively and quantitatively, away from the free ends. At the free ends however, FE model results were sensitive to the mesh density and failed to satisfy the equilibrium and boundary requirements due to the stress singularity. Nevertheless, at the free ends the FE results were qualitatively the same as those of the present model.

Under the same thermal cycling load, it was found that a linear (viscous) creep constitutive law for the solder causes less creep accumulation, much higher stress relaxation, less creep damage, and faster cyclic stabilization and shakedown than the non-linear creep law. The trilayer aspect ratio affects the magnitude and distribution of interfacial stresses as well as the extent of creep damage, particularly at the free ends.

The model can be extended to include external loads and other boundary conditions representative of solder or adhesive joints in larger structures.

Acknowledgements

The authors are grateful for the financial support of the Center for Microelectronics Assembly and Packaging (CMAP).

Appendix A. Creep compliance of a shear loaded strip

A.1. Plane stress condition

Fig. A1 shows a rectangular body of thickness h and length $L = 2l$ subjected to a uniformly distributed shear stress, $\tau(x)$. It is assumed that the boundaries are restrained against any vertical creep displacement (i.e. no bending), supplying pure horizontal deformation to the borders.

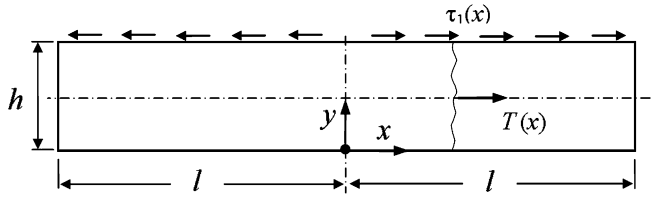

Fig. A1. Two-dimensional rectangular body subject to antisymmetric shear stress on top.

The stress field in this body is characterized upon finding the Airy stress function, $\Phi(x,y)$, from the following bi-harmonic differential equation.

$$\nabla^4 \Phi = 0 \tag{A.1}$$

under the boundary conditions of

$$\tau_{xy}(x,0) = 0, \quad \tau_{xy}(x,h) = \tau(x) = \sum_{k=1,3,5,\ldots}^{\infty} \gamma_k \alpha_k \sin \alpha_k x \tag{A.2}$$

$$w_C(\pm l, y) = w_C(x,0) = w_C(x,h) = 0 \tag{A.3}$$

where $\alpha_k = \frac{k\pi}{2l}$ and $\gamma_k = \frac{2}{\alpha_k l} \int_0^l \tau(x) \sin \alpha_k x \, dx$. As seen in Ghorbani and Spelt (2005), the following Fourier solution to Eq. (A.1) may be sought:

$$\Phi(x,y) = \sum_{k=1,3,5,\ldots}^{\infty} \gamma_k [(A_k + B_k y) \cosh \alpha_k y + (C_k + D_k y) \sinh \alpha_k y] \cos \alpha_k x \tag{A.4}$$

where A_k, B_k, C_k, and D_k are integration constant. The stresses may then be defined as

$$\sigma_x(x,y) = \frac{\partial^2 \Phi}{\partial y^2}, \quad \sigma_y(x,y) = \frac{\partial^2 \Phi}{\partial x^2}, \quad \tau_{xy}(x,y) = -\frac{\partial^2 \Phi}{\partial x \partial y} \tag{A.5}$$

Applying the stress boundary conditions in Eq. (A.2), we find:

$$B_k + \alpha_k C_k = 0 \tag{A.6}$$

$$u_k D_k \cosh u_k + (\alpha_k A_k + u_k B_k + D_k) \sinh u_k = 0 \tag{A.7}$$

where $u_k = \alpha_k h$. Assuming linear creep and plane stress, the creep strain rates can be related to the stresses as follows (Eqs. (1)–(4)):

$$\dot{\varepsilon}_x(x,y) = \frac{\partial \dot{u}_C}{\partial x} = \frac{1}{\beta}(\sigma_x - 0.5\sigma_y) \tag{A.8}$$

$$\dot{\varepsilon}_y(x,y) = \frac{\partial \dot{w}_C}{\partial y} = \frac{1}{\beta}(\sigma_y - 0.5\sigma_x) \tag{A.9}$$

$$\dot{\varepsilon}_{xy}(x,y) = \frac{\partial \dot{u}_C}{\partial y} + \frac{\partial \dot{w}_C}{\partial x} = \frac{3}{\beta}\tau_{xy} \tag{A.10}$$

Integrating Eqs. (A.8) and (A.9) with respect to x and y, respectively, yields:

$$\dot{u}_C(x,y) = \frac{1}{2}\frac{1}{\beta} \sum_{k=1,3,5,\ldots}^{\infty} \gamma_k ([3\alpha_k(A_k + B_k y) + 4D_k] \cosh \alpha_k y + [4B_k + 3\alpha_k(C_k + D_k y)] \sinh \alpha_k y) \sin \alpha_k x + f_1(y) \tag{A.11}$$

$$\dot{w}_C(x,y) = \frac{1}{2}\frac{1}{\beta} \sum_{k=1,3,5,\ldots}^{\infty} \gamma_k ([B_k - 3\alpha_k(C_k + D_k y)] \cosh \alpha_k y + [-3\alpha_k(A_k + B_k y) + D_k] \sinh \alpha_k y) \cos \alpha_k x + f_2(x) \tag{A.12}$$

where f_1 and f_2 are as yet unknown functions of y only and x only, respectively. Substituting these values of $\dot{u}_C$ and $\dot{w}_C$ in Eq. (A.10) we find:

$$f_1'(y) + f_2'(x) = 0 \tag{A.13}$$

As well, $f_2(x)$ must be zero since $w_C(\pm l, y)$ and accordingly its time rate are zero under constant load (Eq. (A.3)). From Eq. (A.13), the fact that horizontal creep displacements are unrestrained, and that the applied shear load is self-equilibrating (i.e. the closed integral of the given load from $-l$ to l is always zero), it can be established that $f_1(y)$ must be constant and equal to zero too. Finally, the last two boundary requirements in Eq. (A.3) yield:

$$B_k + 3\alpha_k C_k = 0 \tag{A.14}$$

$$(\alpha_k A_k + u_k B_k) = (u_k - 1) D_k \coth u_k \tag{A.15}$$

Eqs. (A.6), (A.7), (A.14) and (A.15) determine the constants of integration as

$$A_k = \frac{1 - 3u_k \coth u_k}{4\alpha_k \sinh u_k}, \quad B_k = C_k = 0, \quad D_k = \frac{3}{4}\frac{1}{\sinh u_k} \tag{A.16}$$

Substituting these values into Eq. (A.11), the rate of longitudinal creep displacement at top of this rectangular body, $\dot{u}_C(x,h)$, is derived as

$$\dot{u}_C(x,h) = \frac{3}{8}\frac{1}{\beta}\sum_{k=1,3,5,\ldots}^{\infty} \gamma_k[(5 - 3u_k \coth u_k)\coth u_k + 3u_k]\sin \alpha_k x \tag{A.17}$$

Alternatively, $\dot{u}_C(x,h)$ may be approximated by

$$\dot{u}_C(x,h) = -\frac{3}{4}\frac{1}{\beta h}\int_0^x T(\xi)\,\mathrm{d}\xi + \eta_C \tau(x) \tag{A.18}$$

Considering the series expansion of $\coth u_k$, i.e. $\frac{1}{u_k} + \frac{u_k}{3} - \frac{u_k^3}{45} + \mathrm{o}[u_k]^4$, it is clear that the axial creep compliance $\lambda_C = \frac{3}{4}\frac{1}{\beta h}$ was chosen to cancel out the term $\frac{1}{u_k}$ in Eq. (A.17). Substituting $\tau(x)$ in Eq. (A.18) from Eq. (A.2), comparing the resultant expression with Eq. (A.17), and limiting the analysis to the first term, we find

$$\eta_C = \frac{3}{8\pi}\left[(5 - 3\bar{u}\coth \bar{u})\coth \bar{u} + 3\bar{u} - \frac{2}{\bar{u}}\right]\frac{L}{\beta} \tag{A.19}$$

where $\bar{u} = \pi h/L$. In the case of relatively small and large aspect ratios, $\coth \bar{u}$ approaches $\frac{1}{\bar{u}} + \frac{\bar{u}}{3}$ and unity, respectively, and Eq. (A.19) may be therefore simplified to

$$\eta_C = \frac{h}{\beta} \quad (h/L \leqslant 0.2) \tag{A.20}$$

$$\eta_C = \frac{15}{8\pi}\frac{L}{\beta} \quad (h/L \geqslant 0.7) \tag{A.21}$$

Finally, the total accumulated creep deformation at interfacial points in horizontal direction under the time-independent stress $\tau(x)$ can be defined as

$$u_C(x,h,t) = \int_0^t \dot{u}_C(x,h)\,\mathrm{d}t = \left[-\frac{3}{4}\frac{1}{\beta h}\int_0^x T(\xi)\,\mathrm{d}\xi + \eta_C \tau(x)\right]t \tag{A.22}$$

Note that creep deformation is zero at time zero. In case of time-dependent loading, i.e. when $\tau(x)$ and β, and hence $T(x)$ and η_C, are a function of time, Eq. (A.22) will be as follows:

$$u_C(x,h,t) = \int_0^t \left[-\frac{3}{4}\frac{1}{\beta(s)h}\int_0^x T(\xi,s)\,\mathrm{d}\xi + \eta_C(s)\tau(x,s)\right]\mathrm{d}s \tag{A.23}$$

This expression was used in Eqs. (21)–(24).

A.2. Plane strain condition

Under plane strain condition, normal creep strain rates are as follows (Eqs. (1)–(4)):

$$\dot{\varepsilon}_x(x,y) = \frac{\partial \dot{u}_C}{\partial x} = \frac{3}{4}\frac{1}{\beta}(\sigma_x - \sigma_y) \tag{A.24}$$

$$\dot{\varepsilon}_y(x,y) = \frac{\partial \dot{w}_C}{\partial y} = \frac{3}{4}\frac{1}{\beta}(\sigma_y - \sigma_x) \tag{A.25}$$

and the shear strain rate will remain unchanged (Eq. (A.10)). Following the same procedure as that described for the plane stress condition above, we find the rate of longitudinal creep displacement at top of the rectangular body, $\dot{u}_C(x,h)$, as follows:

$$\dot{u}_C(x,h) = \frac{3}{2}\frac{1}{\beta}\sum_{k=1,3,5,\ldots}^{\infty} \gamma_k[(1-u_k\coth u_k)\coth u_k + u_k]\sin\alpha_k x \tag{A.26}$$

Substituting for $\coth u_k$ with its series expansion in Eq. (A.26), it can be seen that $\dot{u}_C(x,h)$ does not contain the term $\frac{1}{u_k}$, consequently $\lambda_C = 0$. The alternative solution in Eq. (A.18) is therefore simplified to

$$\dot{u}_C(x,h) = \eta_C\tau(x) \tag{A.27}$$

In other words, under plane strain condition and without any bending, the horizontal creep strain rate is in linear proportion to the interfacial shear stress only. Substituting $\tau(x)$ in Eq. (A.27) from Eq. (A.2), comparing the resultant expression with Eq. (A.26), and limiting the analysis to the first term, we find

$$\eta_C = \frac{3}{2\pi}[(1-\bar{u}\coth\bar{u})\coth\bar{u} + \bar{u}]\frac{L}{\beta} \tag{A.28}$$

which in the case of relatively small and large aspect ratios becomes simplified to

$$\eta_C = \frac{h}{\beta} \quad (h/L \leqslant 0.2) \tag{A.29}$$

$$\eta_C = \frac{3}{4\pi}\frac{L}{\beta} \quad (h/L \geqslant 0.7) \tag{A.30}$$

Comparing compliances obtained for both plane stress and plane strain conditions, it is evident that for elongated strips the shear creep compliance η_C is insensitive to plane stress and plane strain conditions, whereas λ_C shows a strong sensitivity. The total horizontal creep accumulated at interfacial points can also be defined as

$$u_C(x,h,t) = \eta_C\tau(x)t \tag{A.31}$$

In the case of time-dependent loading, Eq. (A.31) will be as follows:

$$u_C(x,h,t) = \int_0^t \eta_C(s)\tau(\xi,s)\,\mathrm{d}s \tag{A.32}$$

Appendix B. Creep compliance of a compressed strip

B.1. Plane stress condition

The through-thickness linear creep compliance of a 2D rectangular body (Fig. A1) can be obtained in the similar manner as its shear compliance. It is assumed that the body is subjected to a self-equilibrating pressure, $p(x)$, on top and the boundaries are constrained against any horizontal movements (i.e. no bending). In other words,

$$\sigma_y(x,0) = 0, \quad \sigma_y(x,h) = p(x) = \sum_k^{\infty}\gamma_k\alpha_k\cos\alpha_k x \tag{B.1}$$

$$u_C(\pm l,y) = u_C(x,0) = u_C(x,h) = 0 \tag{B.2}$$

where $\alpha_k = \frac{k\pi}{l}$ and $\gamma_k = \frac{2}{\alpha_k l}\int_0^l p(x)\cos\alpha_k x\,\mathrm{d}x$. As seen in Ghorbani and Spelt (2005), a Fourier solution for the bi-harmonic Eq. (A.1) may be sought as follows:

$$\Phi(x,y) = \sum_k^{\infty}\gamma_k[(A_k + B_k y)\cosh\alpha_k y + (C_k + D_k y)\sinh\alpha_k y]\cos\alpha_k x \tag{B.3}$$

Following the same procedure as that described in Appendix A, the rate of vertical creep deformation at the top of the strip, $\dot{w}_C(x,h)$, may be determined as follows:

$$\dot{w}_C(x,h) = \frac{3}{8}\frac{1}{\beta}\sum_k^{\infty}\gamma_k[(5+3w_k\coth w_k)\coth w_k - 3w_k]\cos\alpha_k x \tag{B.4}$$

where $w_k = \alpha_k h$. Alternatively, $\dot{w}_C(x,h)$ (in the absence of bending) can be described by

$$\dot{w}_C(x,h) = -\frac{3}{\beta h}\int_{-l}^{x} V(\xi)\,d\xi + \delta_C p(x) \tag{B.5}$$

Note again that the choice of shear compliance $\mu_C = \frac{3}{\beta h}$ was made to cancel out the $\frac{1}{w_k}$ term in the expanded form of Eq. (B.4). Differentiating Eqs. (B.4) and (B.5), comparing them, and limiting the analysis to the first term, it is found that

$$\delta_C = \frac{3}{16\pi}\left[(5 + 3\bar{w}\coth\bar{w})\coth\bar{w} - 3\bar{w} - \frac{8}{\bar{w}}\right]\frac{L}{\beta} \tag{B.6}$$

where $\bar{w} = \pi h/l$. In the case of small and large aspect ratios, Eq. (B.12) may be simplified to

$$\delta_C = \frac{1}{4}\frac{h}{\beta} \quad (h/l \leqslant 0.2) \tag{B.7}$$

$$\delta_C = \frac{15}{16\pi}\frac{L}{\beta} \quad (h/l \geqslant 0.7) \tag{B.8}$$

The total vertical creep deformation accumulated at interfacial points can therefore be defined as

$$w_C(x,h,t) = \int_0^t \dot{w}_C(x,h)\,dt = \left[\delta_C p(x) - \frac{3}{\beta h}\int_{-l}^{x} V(\xi)\,d\xi\right]t \tag{B.9}$$

In the case of variable loading and material parameters, however, Eq. (B.10) will be as follows:

$$w_C(x,h,t) = \int_0^t \left[-\frac{3}{\beta(s)h}\int_{-l}^{x} V(\xi,s)\,d\xi + \delta_C(s)p(x,s)\right]ds \tag{B.10}$$

This expression was used in Eqs. (34)–(37).

B.2. Plane strain condition

Employing the same method as the plane stress condition, $\dot{w}_C(x,h)$ under plane strain conditions may be defined as

$$\dot{w}_C(x,h) = \frac{3}{2}\frac{1}{\beta}\sum_k^{\infty}\gamma_k[(1 + w_k\coth w_k)\coth w_k - w_k]\cos\alpha_k x \tag{B.11}$$

Consequently, μ_C remains unchanged ($\frac{3}{h\beta}$) and δ_C will be defined as

$$\delta_C = \frac{3}{4\pi}\left[(1 + \bar{w}\coth\bar{w})\coth\bar{w} - \bar{w} - \frac{2}{\bar{w}}\right]\frac{L}{\beta} \tag{B.12}$$

which in the case of small and large aspect ratios becomes simplified to

$$\delta_C \cong 0 \quad (h/l \leqslant 0.2) \tag{B.13}$$

$$\delta_C = \frac{3}{4\pi}\frac{L}{\beta} \quad (h/l \geqslant 0.7) \tag{B.14}$$

Comparing the plane stress and plane strain compliances, it is evident that δ_C is sensitive to these conditions and transverse shear compliance μ_C is not sensitive at all. Total vertical creep deformation accumulated at interfacial points can also be calculated from Eqs. (B.9) and (B.10) for constant and time-dependent loading, respectively.

References

Akay, H.U., Paydar, N.H., Bilgic, A., 1997. Fatigue life predictions for thermally loaded solder joints using a volume-weighted averaging technique. Journal of Electronic Packaging 119, 228–235.

ANSYS 8.0, 2003. ANSYS, Inc, Canonsburg, PA.

Basaran, C., Zhao, Y., 2001. Mesh sensitivity and FEA for multi-layered electronic packaging. Journal of Electronic Packaging 123, 218–224.
Bogy, D.B., 1968. Edge-bonded dissimilar orthogonal elastic wedges under normal and shear loadings. Journal of Applied Mechanics 33, 460–466.
Bruno, J., Destrebecq, J.F., Vergne, A., 1999. Incremental analysis of time-dependent effects in composite structures. Computers and Structures 73, 425–435.
Chen, D., Cheng, S., Gerhardt, T.D., 1982. Thermal stresses in laminated beams. Journal of Thermal Stresses 5, 67–84.
Chen, T.C., Wu, H.C., Lin, C.L., 2003. Longitudinal anisotropic stress and deformation in multilayered film heterostructures due to lattice misfit. Journal of Crystal Growth 249, 44–58.
Compaq Visual FORTRAN 6.6, 2000. Compaq Computer Corporation, Houston, Texas.
Dillard, D.A., Guo, S., Chen, B., Yu, J.H., 2003. Adhesive layer shrinkage in bonds subjected to thermal cycling. Mechanics of Time-Dependent Materials 7, 21–39.
Dowling, N.E., 1999. Mechanical Behavior of Materials. Prentice-Hall Inc, NJ, USA.
Dutta, I., Peterson, K.A., Park, C., 2003. Interfacial creep in multi-component material systems. JOM 55 (1), 38–43.
Eslami, M.R., Mahbadi, H., 2001. Cyclic loading of thermal stresses. Journal of Thermal Stresses 24, 577–603.
Findley, W.N., Cho, U.W., Ding, J.L., 1979. Creep of metals and plastics under combined stress, a review. Journal of Engineering Materials and Technology 101, 365–368.
Ghorbani, H.R., Spelt, J.K., 2005. Interfacial thermal stresses in trilayer assemblies. Journal of Microelectronic Packaging 127 (3), 314–323.
Glaser, J.C., 1990. Thermal stresses in compliantly joined materials. Journal of Electronic Packaging 112, 24–29.
Hayashi, T., 1967. Analytical study of interlaminar shear stresses in a laminated composite plate. Transactions of the Japan Society for Aeronautical and Space Sciences 10 (17), 43–48.
Hibbeler, R., Mura, T., 1969. Viscous creep ratcheting of nuclear reactor fuel element. Nuclear Engineering and Design 9, 131–143.
Humfeld, G.R., Dillard, D.A., 1998. Residual stress development in adhesive joints subjected to thermal cycling. Journal of Adhesion 65, 277–306.
Lee, S.S., Kim, N., 2004. Interfacial stresses in viscoelastic thin layer due to moisture absorption. Advances in Nondestructive Evaluation. Key Engineering Materials 270–273 (1), 843–848.
Lewis, A.C., Van Heerden, D., Josell, D., Weihs, T.P., 2003. Creep deformation in multilayered and microlaminate materials. Journal of the Minerals, Metals and Materials Society 55 (1), 34–37.
Mackerle, J., 2002. Finite element analysis and simulation of adhesive bonding, soldering and brazing – an addendum: a bibliography (1996–2002). Modeling and Simulation in Materials Science and Engineering 10, 637–671.
Madras, C.G., Wong, P.Y., Miaoulis, I.N., 1996. Viscoelastic deformation during thermal cycling of adhesively bonded optical coatings. Materials Letters 28, 21–26.
Matsunaga, H., 2004. A comparison between 2-D single-layer and 3-D layerwise theories for computing interlaminar stresses of laminated composite and sandwich plates subjected to thermal loadings. Composite Structures 64, 161–177.
Mirman, I.B., 1991. Effect of peeling stresses in bimaterial assembly. Journal of Microelectronic Packaging 113, 431–433.
Mirman, B.A., Knecht, S., 1990. Creep strains in elongated bond layer. IEEE Transactions on Components, Hybrids, and Manufacturing Technology 13 (4), 914–928.
Qi, Y., Zbrzezny, A.R., Agia, M., Lam, R., Ghorbani, H.R., Snugovsky, P., Spelt, J.K., 2004. Accelerated thermal fatigue of lead-free solder joints as a function of reflow cooling rate. Journal of Electronic Materials 33 (12), 1497–1506.
Qi, Y., Lam, R., Ghorbani, H.R., Snugovsky, P., Spelt, J.K., 2006. Temperature profile effects in accelerated thermal cycling of SnPb and Pb-free solder joints. Microelectronics Reliability 46, 574–578.
Ru, C.Q., 2002. Interfacial thermal stresses in bimaterial elastic beams: modified beam models revisited. Journal of Electronic Packaging 124, 141–146.
Shen, Y.L., Suresh, S., 1995. Elastoplastic deformation of multilayered materials during thermal cycling. Materials Research Society 10 (5), 1200–1215.
Shen, Y.L., Suresh, S., 1996. Steady-state creep of metal–ceramic multilayered materials. Acta Materialia 44 (4), 1337–1348.
Suhir, E., 1986. Calculated thermally induced stresses in adhesively bonded and soldered assemblies. In: Int. Symp. on Microelectronics Proc., Atlanta, October, Int. Soc. for Hybrid Microelectronics, Reston, VA, USA, pp. 383–392.
Suhir, E., 2001. Analysis of interfacial thermal stresses in a trimaterial assembly. Journal of Applied Physics 89 (7), 3685–3694.
Wang, W.C., Lin, J.C., 2003. Photoelastic investigation of bimaterial interfacial stresses induced by thermal loading. Strain 39, 143–148.
Wang, K.P., Huang, Y.Y., Chandra, A., Hu, K.X., 2000. Interfacial shear stress, peeling stress, and die cracking stress in trilayer electronic assemblies. IEEE Transactions on Components and Packaging Technologies 23 (2), 309–316.
Wen, Y., Basaran, C., 2004. An analytical model for thermal stress analysis of multi-layered microelectronic packaging. Mechanics of Materials 36, 369–385.
Xie, W., Sitaraman, S.K., 2000. Interfacial thermal stress analysis of anisotropic multi-layered electronic packaging structures. Journal of Electronic Packaging 122, 61–66.
Yang, F., 1997. Creep due to grain boundary diffusion and grain boundary viscous flow. Journal of Physics D: Applied Physics 30, 286–288.
Yin, W.L., 1991. Thermal stresses and free-edge effects in laminated beams: a variational approach using stress functions. Journal of Electronic Packaging 113, 68–75.
Zeyfang, R., 1971. Stress and strains in a plate bonded to a substrate: semiconductor devices. Solid-State Electronics 14, 1035–1039.